In situ and high-resolution Cryo-EM structure of the Type VI secretion membrane complex

Chiara Rapisarda, Yassine Cherrak, Romain Kooger, Victoria Schmidt, Riccardo Pellarin, Laureen Logger, E. Cascales, Martin Pilhofer, Eric Durand, Rémi Fronzes

In situ and high-resolution Cryo-EM structure of the Type VI secretion membrane complex

Chiara Rapisarda[1,2]*, Yassine Cherrak [3]*, Romain Kooger[4]*, Victoria Schmidt[3], Riccardo Pellarin[5], Laureen Logger[3], Eric Cascales[3], Martin Pilhofer[4#], Eric Durand[6#], Rémi Fronzes[1,2#]

[1]CNRS UMR 5234 Microbiologie Fondamentale et Pathogénicité, Paris, France.
[2]Institut Européen de Chimie et Biologie, University of Bordeaux, 2 rue Robert Escarpit, 33607, Pessac, France.
[3]Laboratoire d'Ingénierie des Systèmes Macromoléculaires (LISM), Institut de Microbiologie de la Méditerranée (IMM), UMR7255, Aix-Marseille Université - CNRS, Marseille, France.
[4]Institute of Molecular Biology & Biophysics, Eidgenössische Technische Hochschule Zürich, CH-8093 Zürich, Switzerland
[5]Institut Pasteur, Structural Bioinformatics Unit, Department of Structural Biology and Chemistry, CNRS UMR 3528, C3BI USR 3756, Paris, France.
[6]Laboratoire d'Ingénierie des Systèmes Macromoléculaires (LISM), Institut de Microbiologie de la Méditerranée (IMM), UMR7255, INSERM - Marseille, France.

*these authors contributed equally to the work
[#] corresponding authors: pilhofer@biol.ethz.ch, edurand@imm.cnrs.fr & edurand@inserm.fr and r.fronzes@iecb.u-bordeaux.fr

Abstract

Bacteria have evolved macromolecular machineries that secrete effectors and toxins to survive and thrive in diverse environments. The type VI secretion system (T6SS) is a contractile machine that is related to *Myoviridae* phages. It is composed of a phage tail-like structure inserted in the bacterial cell envelope by a membrane complex (MC) comprising the TssJ, TssL and TssM proteins. We previously reported the low-resolution negative-stain electron microscopy structure of the enteroaggregative *Escherichia coli* MC, and proposed a rotational 5-fold symmetry with a TssJ:TssL:TssM stoichiometry of 2:2:2. Here, cryo-electron tomography analyses of the T6SS MC confirm the 5-fold symmetry *in situ* and identify the regions of the structure that insert into the bacterial membranes. A high-resolution model obtained by single particle cryo-electron microscopy highlights new features: five additional copies of TssJ, yielding a TssJ:TssL:TssM stoichiometry of 3:2:2, an 11-residue loop in TssM, protruding inside the lumen of the MC and constituting a functionally important periplasmic gate, and hinge regions. Based on these data, we propose an updated model on T6SS structure, assembly and function.

Introduction:

In a competitive environment, the ability to communicate and outcompete neighbours provides bacteria with key advantages to survive. The type VI secretion system (T6SS) is a macromolecular complex involved in the release of toxins that disrupt essential functions in competitor cells (Russell *et al*, 2014). The T6SS is associated with increased survival and pathogenicity in bacteria expressing it (Zhao *et al*, 2018). It is composed of 13-14 core proteins (Boyer *et al*, 2009), usually encoded in the same locus in the genome (Mougous *et al*, 2006). The T6SS assembles a molecular spring-loaded dagger, which punctures the target cell to secrete fully folded effector proteins into neighbouring bacteria (Russell *et al*, 2011) or eukaryotic hosts (Hachani *et al*, 2016) The full assembly consists of the trans-envelope TssJLM membrane complex (MC) (Durand *et al*, 2015) that tethers the TssKFGE-VgrG baseplate (Brunet *et al*, 2015)(Cherrak *et al*, 2018), onto which the tail polymerizes. This tail comprises the inner tube made of stacks of Hcp hexamers wrapped by the TssBC sheath proteins that polymerize in a helical conformation (Robb *et al*, 2013; Brunet *et al*, 2014; Clemens *et al*, 2015; Kudryashev *et al*, 2015; Chang *et al*, 2017; Wang *et al*, 2017), and tipped by the spike VgrG, which can be sharpened by the PAAR protein (Renault *et al*, 2018; Shneider *et al*, 2013). Effectors are either associated within the Hcp lumen, or directly or indirectly bound to the VgrG or PAAR spike (Unterweger *et al*, 2017; Silverman *et al*, 2013; Shneider *et al*, 2013; Flaugnatti *et al*, 2016; Quentin *et al*, 2018). Upon contact with a neighbouring cell, unknown signals trigger the contraction of the sheath causing the tube and spike to pierce the membranes of the target cell, hence delivering the effectors (Basler *et al*, 2012).

While the baseplate, tube and sheath proteins are conserved among contractile injection systems, the MC is specific to the T6SS. TssJ is an outer membrane lipoprotein (Aschtgen *et al*, 2008a) that positions first at the site of assembly, and then recruits TssM and TssL (Durand *et al*, 2015). TssM and TssL are two inner membrane proteins that share homology with two accessory subunits associated with Type IV secretion system (T4SS)b, IcmF and IcmH/DotU (Aschtgen *et al*, 2012; Ma *et al*, 2009; Durand *et al*, 2012; Logger *et al*, 2016). Not only does the MC anchor the baseplate to the inner membrane, but it also serves as a channel to allow the passage of the tail tube/spike, and to maintain the integrity of the attacking cell during the translocation of the inner tube (Durand *et al*, 2015). The different subunits and the MC have been extensively biochemically characterised and several crystal structures of the components are available from various bacterial species (Robb *et al*, 2013; Felisberto-Rodrigues *et al*, 2011; Durand *et al*, 2012; Rao *et al*, 2011; Robb *et al*, 2012; Chang & Kim, 2015; Durand *et al*, 2015). We previously reported the negative-stain electron microscopy (EM) structure of the TssJLM complex from enteroaggregative *Escherichia coli* (EAEC). We determined that 10 TssJ lipoproteins are bound to 10 TssM proteins, forming two

72 concentric rings of pillars and arches that span the periplasm. The arches were shown to link to a
73 flexible base composed of the N-terminal part of TssM and 10 copies of TssL (Durand *et al*, 2015).
74 This study also revealed that the EAEC TssJLM complex assembles into a 5-fold rotationally
75 symmetric trans-envelope structure. However, the symmetry mismatch between the 5-fold
76 symmetry of the MC and 6-fold symmetry of the baseplate (Nazarov *et al*, 2018) raised questions on
77 whether the purified TssJLM MC reflects the *in vivo* situation. In addition, although most of the
78 available crystal structures can be readily fitted into this EM structure, we currently lack molecular
79 details on the whole complex, such as the precise location of the membranes, of the trans-
80 membrane helices, and the potential presence of a periplasmic channel.
81 Here, we first present the *in situ* cryo-electron tomography (cryo-ET) structure of the EAEC
82 TssJLM MC. These data confirm the 5-fold symmetry of the complex *in vivo*, and provide information
83 on the location of the inner and outer membranes. We then present the single particle (SPA) cryo-
84 electron microscopy (cryo-EM) structure of the MC that describes the molecular architecture of the
85 periplasmic portion of the complex. This high-resolution cryo-EM structure reveals the presence of
86 five additional copies of TssJ at the tip of the complex, and provides detailed structural information
87 on the periplasmic gate that narrows the MC channel. Finally, we demonstrate that this periplasmic
88 gate and the additional TssJ are required for T6SS-dependent activity *in vivo*.

89 ## Results

90 ### *Structure of the T6SS MC within the cell envelope*

91 To observe the T6SS MC in its native cellular environment, we performed cryo-ET on bacterial
92 cells (Weiss *et al*, 2017). With the aim to have a sufficient number of particles to obtain an *in situ*
93 structure by subtomogram averaging, we imaged *E. coli* BL21(DE3) cells in which TssJLM were
94 heterologously overproduced. This strain does not possess T6SS genes, thereby preventing any
95 crosstalk or protein-protein interactions between TssJLM and other natively present T6SS proteins.
96 Since *E. coli* is too thick to be directly imaged by cryo-ET, we pursued three different approaches to
97 tackle sample thickness. The first approach consisted of engineering a minicell-producing skinny
98 strain (Farley et al, 2016) of *E. coli* BL21(DE3), and thereby generating a minicell strain that is
99 compatible with the T7-based expression system. Although this strain produced minicells as small as
100 450 nm in diameter (Fig EV1A), their size still affected the contrast to an extent that did not allow for
101 sub-tomogram averaging. Nevertheless, characteristic inverted Y-shaped particles (side views, Fig
102 EV1B) and star-shaped particles (top views, Fig EV1C) could occasionally be observed in the
103 periplasm of these minicells. In a second approach, tomograms were recorded of cells that were
104 partially lysed and exhibited a high contrast (Fig EV1D, E). These cells, which have previously been

described as “ghost cells” due to their transparent appearance, still had mostly intact membranes and showed their cytoplasmic macromolecular complexes such as ribosomes (Fu *et al*, 2014). In a third approach, we used a state-of-the-art cryo-sample thinning method called focused ion beam (FIB) milling to thin *E. coli* BL21(DE3) cells in which TssJLM were heterologously overproduced (Fig EV1F, G). FIB milling allows to etch through a lawn of bacterial cells and to thin them down to under 200 nm (Medeiros *et al*, 2018a, 2018b; Marko *et al*, 2007). This approach was more native, as it was performed on intact rod-shaped wild-type BL21(DE3) cells. These tomograms had a high contrast and provided great detail. To confirm the relevance of these observations, we carried out control experiments in the native T6SS^{+} EAEC 17-2 strain. TssJLM particles were frequently observed by cryo-ET, both when heterologously overproduced (Fig EV1H, note that the particles could occasionally be found detached from the outer membrane: Fig EV1J) as well as under native conditions, *i.e.* in wild-type EAEC 17-2 cells (Fig EV1I).

Sub-volumes of star-shaped (top views) and inverted Y-shaped (side views) particles were manually picked, computationally extracted, and subsequently aligned and averaged. The resulting average was similar to the *in vitro* T6SS MC structure published previously (Durand *et al*, 2015), with a tip and a core, made of 5 pairs of pillars forming a narrow central channel, that splits into 10 arches (Fig 1A-E). Importantly, the 5-fold symmetry was evident without applying symmetry (Fig 1A’). As it is the case for the TssJLM MC solved by EM (Durand *et al*, 2015), the periplasmic core and the arches were well resolved, whereas the inner membrane-embedded base and the outer membrane-embedded cap were poorly resolved. The Fourier shell correlation (FSC) curve indicated a resolution of 25 Å at a coefficient of 0.5 (Appendix Fig S1 A). The prevalence of top views indicated that the average might be affected by a missing wedge (Appendix Fig S1B).

After aligning and averaging a set of sub-volumes, it can be useful to place the isosurface of the average back in the original tomographic volume to analyze the positions and orientations of the individual aligned particles. In this way, we obtained a clear view of the location of the MC within the cell envelope (Fig 2A, Movie 1 and Appendix Fig S1C-E, Movie 2). The position of the membranes with respect to the TssJLM highlighted that the tip was embedded in the outer membrane without crossing it, while the MC was anchored in the inner membrane at the lower part of the arches (Fig 2B). In some cases, densities could be seen spanning the inner membrane and extending into the cytoplasm (Fig 2C). In what could be an overproduction artefact, TssJLM particles were also found in cytoplasmic membrane invaginations (Fig 2A). Altogether, these data confirmed the 5-fold symmetry of the T6SS TssJLM MC *in situ* and provided further insights into the position of the inner and outer membranes.

Structural analysis of the TssJLM complex by cryo-EM

We previously reported the negative stain EM structure of the EAEC TssJLM MC (Durand *et al*, 2015). Here, we used the same purification procedure and performed SPA cryo-EM to obtain the cryo-EM structure of the 1.7-MDa T6SS MC at 4.9 Å overall resolution. With a 5-fold symmetry imposed, the local resolution ranged between 4.1 Å and 21.7 Å (Fig 3A and Appendix Fig S2A-F).

The 5-fold symmetry is clearly visible in the 2D classes top views and the volume slices of the reconstruction, which retain a 5-pointed star shape (Appendix Fig S2C, G). When no symmetry was applied during the reconstruction, the overall resolution decreased to 7.5 Å but the pentameric nature of the complex was maintained, with only one of the 10 arches displaying weaker density than the others causing the drop in resolution (Appendix Fig S2H, I and S3). This could indicate partial assembly of the complex *in vivo* or disassembly during its purification.

The overall structure resembles that obtained by negative stain (Appendix Fig S2J)(Durand *et al*, 2015). The architecture of the complex comprises a tip connected to a core region that extends to a base, through a double ring of pillars with arches in proximity to the inner membrane (Fig 3A-B). Several notable features are already evident from the cryo-EM density map of the full complex (Fig 3A). First, the tip region and the base are disordered, and appear to be filled by random densities. Second, cross-sections of the full complex, show that the channel, across which tube/spike transport might occur, is closed by a gate at the intersection between arches and pillars, above the inner membrane (Fig 3B-E and Appendix Fig S3A-D respectively). This gate is also visible in the reconstruction without symmetry applied (Appendix Fig S2H and S3).

To better characterise the flexibility of the base of the complex, we collected tomograms on the same frozen EM grids that were used to collect the SPA dataset (Appendix Fig S4A-C). The base of individual complexes appeared as very heterogeneous, with single arches often pointing in opposite directions, or on the contrary several arches clumping together (Appendix Fig S4A). On the other hand, the core was rigid and resembled a 5-branched star. Moreover, about 20% of the particles possessed only 3 or 4 out of 5 branches (Appendix Fig S4B), indicating that partial assemblies could be stable. The particles were lying in a thin layer of ice (25 nm) and were found in different orientations (Appendix Fig S4C).

The structure of the base

To try and overcome the inherent flexibility of the complex and better discern different features of the base, we performed a density subtraction of the tip, core and arches followed by a focused refinement of the base with and without symmetry applied. We thus obtained 2D classes and a 3D structure of the base at 17-Å resolution when a C5 symmetry was applied (Fig 3F and

Appendix Fig S4E-F). When observing the cross section of the base in the full complex, as indicated by arrows in Fig3B, and in the subtracted structure (Appendix Fig S4E), two 110 Å-wide linear densities are clearly visible, separated by 40 Å. This double layer of density is consistent with the density diagram of a lipid bilayer with the head groups being the most dense at a distance of ~4 nm from each other and fits well a lipid bilayer composed of PE, obtained using the CHARMM-GUI (Jo *et al*, 2007) (Appendix Fig S4E). We propose that the inner membrane sub-domain of the T6SS MC could be filled by a lipid bilayer. However, such hypothesis will have to be further explored in the future.

An additional TssJ is present in the full complex

To focus on the best-resolved region of the cryo-EM map, the base was subtracted from the tip, a 2D classification and a masked 3D refinement was performed to obtain the structure of the core at 4.5 Å (Figs 3G and EV2A-B), with a local resolution ranging from 4 Å to >10 Å (Fig EV2C). The known crystallographic structure of the C-terminus of TssM (aa. 869-1129) bound to TssJ (PDB 4Y7O) could be easily fitted in the outer and inner pillars, with a correlation of 0.8505 and 0.565 respectively, leaving an extra density (Fig EV2D-E). Interestingly, an extra TssJ subunit, TssJ', which was not observed in the low resolution complex (Durand *et al*, 2015) fits in this extra density with a correlation of 0.879 (EV2E-F). We thus conclude that the T6SS MC comprises 15 TssJ proteins, and 3 TssJs for 2 TssM (Fig 4A). No additional residues were visible for the N- and C-termini of TssJ (1-21 and 151-155), disordered in both the crystal and the cryo-EM structures. After placing the extra TssJ, we refined the TssM-TssJ crystal structure and the newly fitted TssJ copy against the cryo-EM map to obtain the structure of each TssM and TssJ monomer within the whole MC.

TssJ' binds to the MC through previously unknown interfaces. If we consider TssJ' and the TssJ subunits from the inner and outer pillars (TssJ.i and TssJ.o, respectively) (Figs 4A-C and EV3A-B) with TssJ.i and TssJ.o being in contact with TssM.i and TssM.o respectively, they sit in the same position as in the crystal structure and in the outer and inner pillars (Fig 4B). By contrast, TssJ' binds to TssM.o and TssJ.i strongly (Figs 4C, EV3C , and Table 1). In particular, the interaction of TssJ' with TssJ.i is specifically strong, as their contact is mediated not only by hydrogen bonds but also by salt bridges (R31 with E34, and D97 with R33; see Fig EV3C and Table 1). TssJ' binds to TssM.i via hydrogen bonds only and this interaction is comparable to that between TssJ.i and TssJ.o with TssM.i and TssM.o respectively (surface of interaction 573 $Å^2$ and -2.6 kcal/mol ΔG) (Fig 4B-C, Table 1).

TssJ' is required for MC assembly and T6SS activity

To gain further information on the function and *in vivo* relevance of TssJ', mutations that specifically impact the TssJ'-TssJ.i interface were engineered onto the chromosome, at the native

206 locus. Two residues, R31 and D97 (Fig EV3C), were targeted as they form a salt bridge with E34 and
207 R33 in TssJ.i, respectively (Table 1 and Fig EV3C). The R31E, D97A and D97K substitutions were then
208 tested for their ability to outcompete a fluorescent *E. coli* competitor strain. Although the R31E and
209 D97A did not significantly impact T6SS antibacterial activity, the D97K mutation abolished proper
210 function of the T6SS (Fig 4D). The assembly and stability of the T6SS MC was then assessed by
211 fluorescence microscopy using a chromosomally-encoded and functional fusion protein between
212 TssM and the super-folder GFP ($_{sf\text{GFP}}$TssM, Durand *et al*, 2015) (Appendix Fig S5A). As previously
213 observed, $_{\text{sfGFP}}$TssM formed stable foci (Durand *et al*, 2015). By contrast, cells producing the TssJ
214 D97K variant presented small and unstable fluorescent $_{\text{sfGFP}}$TssM foci (Fig 4E). Time-lapse
215 fluorescence microscopy recordings showed that about 90% of the foci observed in the $_{\text{sfGFP}}$TssM
216 strain (n = 50) are stable over the 600-sec recording time, in agreement with the previous
217 observation that the EAEC T6SS MC is stable and serves for several contraction/elongation cycles
218 (Durand et al., 2015). By contrast, with a mean lifetime of ~ 107 sec (n = 50) the $_{\text{sfGFP}}$TssM fluorescent
219 foci observed in cells producing the TssJ D97K variant are drastically less stable (Fig 4E). We then
220 tested whether the TssJ D97K variant promotes sheath assembly, using chromosomally-encoded
221 functional $_{\text{sfGFP}}$TssB fusion. Contrarily to the wild-type parental cells in which dynamic sheaths can be
222 observed, no sheath polymerization occurs in presence of TssJ-D97K (Appendix Figs S5A-B).
223 Altogether, these results demonstrate that the TssJ'-TssJ.i interface is required for the stability of the
224 T6SS MC, sheath formation and T6SS antibacterial activity.
225

226 ***A flexible hinge within the TssM periplasmic domain***

227 We were able to confidently build *de novo* the periplasmic domain of TssM including its N-
228 terminal fragment (residues 579 to 869) that was missing in the crystal structure (Durand *et al*,
229 2015). This was done in Coot (Emsley *et al*, 2010) by using Phyre2 secondary structure predictions
230 (Kelley *et al*, 2015) and RaptorX residue contact predictions (Källberg *et al*, 2012) as validation tools
231 (Fig 5A and Appendix Fig S6A-C). The cryo-EM structure of the TssM periplasmic domain slightly
232 differs from the X-ray structure (Fig EV4A). From the C-terminus, helix 869-891 extends to amino-acid
233 841 with a slight kink at residue Pro-870. The remaining N-terminal fragment forms an α-helical
234 domain comprising 8 helices that snake back and forth to the inner membrane (Fig 5B). The region
235 closest to the membrane was too flexible to be resolved and for an atomic model to be built
236 (Appendix Fig S6B). The cryo-EM pseudoatomic model of the fully assembled TssM-TssJ complex
237 shows it forms a bell shape composed of two rings of pillars that twist around each other (Fig 5A).
238 Within each asymmetric unit, two copies of TssM are present, named TssM.o in the outer pillar and
239 TssM.i in the inner pillar. The inner and the outer pillar TssM proteins are superimposable with the

exception of a 23° kink located at residue 867 (Fig EV4B). These two TssM subunits interact front-to-back (Fig EV4C) with an area of 1168 Å^2, a binding energy of -9.9 kcal/mol, and a ΔG of -5.2 kcal/mol. Each TssM.i also interacts with two adjacent TssM.i within the inner TssM ring at an angle of 76˚, with an area of 1529 Å^2, a binding energy of -12 kcal/mol and a ΔG of -5.32 kcal/mol (Figs EV3A and EV4D). Finally, TssM.o^{+1} also interacts with TssM.i and the two are oriented at 68° from one another (Figs EV3A and EV4E).

A poorly-defined density that sits in the core region between TssM.i and TssM.o^{+1}, was attributed to the C-terminus of TssM. If we were to build a small loop that terminates into a helix at the C-terminus, we would not be able to reach the membrane region as previously proposed (Durand *et al*, 2015) (Fig EV4F). This same loop is disordered in the outer pillar monomer (TssM.o). Additionally, the resolution of the pillars gets worse towards the basal side, and no secondary structure could be identified when we tried to build *de novo* the atomic model of TssM. Despite this high degree of flexibility, we produced a model of the periplasmic region between amino-acids 390 and 550 based on RaptorX contact predictions. This model fits well (correlations of 0.819 and 0.827) into the remaining densities (Fig EV4G). The EM density shows that while they are separated at the level of the arches, the inner and the outer pillar re-join at the level of the inner membrane (Fig EV4G).

The periplasmic TssM gate

The inner pillars of TssM form a channel with a diameter that varies between 2.6 Å and > 20 Å (Fig 5C). The site of constriction observed in the cryo-EM density (Figs 3B, E) corresponds to loop 776-786 in the atomic model of TssM (Fig 5D). Specifically, residues Gln-779 and Asn-780-781 maintain the constriction via polar interactions (Fig 5D). In the outer pillar, the same loop interacts with loop 600-625 on the neighbouring pillar, providing further stabilisation of the structure (Appendix Fig S7A). Conservation analysis of the sequence with related proteins, predicted by the ConSurf server (Celniker *et al*, 2013), indicated that the sequence of the loop 776-786 is poorly conserved amongst species (Appendix Fig S7B) although the presence of a loop at this position is a conserved feature. As previously proposed (Durand *et al*, 2015), these data suggest that the purified TssJLM MC is in a closed state. Large conformational changes, including modification of the constriction and movement of the inner pillars are therefore required to allow the passage of the tube/spike during sheath contraction.

The TssM periplasmic gate is required for MC assembly.

To test the function of the periplasmic gate, several mutations were engineered at the *tssM* locus in the wild-type EAEC 17-2 strain and the function of the T6SS was assessed as previously described (Fig 5E-G). To covalently stabilize the contacts between the inner pillars and thus prevent MC opening, Q779 and N780 were substituted with cysteines (Q779C-N780C). Conversely, a constitutively open gate was created by deleting a large portion of the constriction loop (Δ777-783). Antibacterial competition assays showed that the Q779C-N780C variant loses the ability to outcompete competitor cells, whereas the single control mutant Q779C did not (Figure 5E). Deletion of the Δ777-783 loop also impaired the T6SS antibacterial activity (Figure 5E). Fluorescence microscopy recordings further showed that $_{sfGFP}$TssM Q779C-N780C and $_{sfGFP}$TssM Δ777-783 do not assemble TssM foci since, in contrast to the parental strain, diffuse fluorescent patterns were observed (Fig 5F and Appendix Fig S8). These results demonstrate that the MC is not properly assembled when the integrity of the periplasmic gate is impacted. As expected, these mutant cells did not assemble T6SS sheaths (Fig 5G and Appendix Fig S8).

Discussion

In this study, we report the *in situ* and *in vitro* structures of the T6SS TssJLM MC from EAEC. The cryo-ET structure confirmed the 5-fold symmetry and general architecture *in vivo*, while the high-resolution cryo-EM structure provided molecular details about the periplasmic portion of the complex (Fig 1, Fig 3 and Movie 3). As previously defined, the pentameric propeller-like structure composed of 10 pillars intertwined with each other was observed both *in situ* and from purified material (Figs 1 and 3C-E). Cryo-ET analyses allowed to position both the inner and outer membranes. As anticipated based on biochemical experiments showing that TssJ is a periplasmic lipoprotein attached to the outer membrane by an acyl anchor (Aschtgen *et al*, 2008), the tip of the complex is embedded in the outer membrane (Fig 2B). However, neither the predicted detergent cap in the SPA cryo-EM structure nor the cryo-ET data, indicate that TssJLM breaches or crosses the outer membrane (Fig 2, Fig 3A-B). Nevertheless, it has been shown that this region is extracellularly exposed in wild-type EAEC cells (Durand *et al*, 2015). Although the cryo-EM structure demonstrates that the C-terminal region of TssM locates in the periplasm, we propose that the recruitment of specific T6SS components induces MC conformational changes and cell surface exposition of the TssM C-terminus. While our previous study suggested that the inner membrane locates at the level of the arches (Durand *et al*, 2015), the cryo-ET analyses revealed that the inner membrane surrounds the base (Fig 2B). Moreover, some tomograms also revealed the most basal parts of the MC, which cross the inner membrane into the cytoplasm (Fig 2A, C). These cytoplasmic densities, which we can assume would be connected to the baseplate in a fully assembled T6SS, had a heterogeneous

appearance that highlighted the flexibility of the base, as discussed below. The *in situ* cryo-ET structure presents an apparent elongation of the tip region compared to the cryo-EM structure (Appendix Fig S9A, B and Movie 3), which could correspond to an additional density associated to the outer membrane, or which could alternatively be explained by the missing wedge. Nevertheless, the similarities between both structures allowed the atomic model of TssJ - TssM to be docked into the *in situ* average (Appendix Fig S9C, D), whereas the cryo-EM structure could be placed in a cellular context (Appendix Fig S9E and Movie 3).

The base of the complex in this higher resolution structure was not better resolved than in the negative stain structure (Fig 3A, F, and Appendix Fig S2D). This base should comprise 10 copies of the TssM and TssL cytoplasmic domains (Durand *et al*, 2015). TssL forms dimers (Zoued *et al*, 2018; Durand *et al*, 2012; Zoued *et al*, 2016), and the crystal structure of its cytoplasmic hook-like domain has been reported from various species including EAEC, *P. aeruginosa* and *V. cholerae* (Durand *et al*, 2012; Robb *et al*, 2012; Chang & Kim, 2015; Wang *et al*, 2018). The TssM cytoplasmic domain is comprised between the N-terminal transmembrane hairpin and a third transmembrane helix (Ma *et al*, 2009; Logger *et al*, 2016). No high-resolution structure of the TssM cytoplasmic domain is available, although a model has been built based on homology with DPY-30 and NTPases (Logger *et al*, 2016). Unfortunately, due to the poor resolution of the base, we did not succeed to confidently fit the TssL and TssM cytoplasmic domains in this density. Additional assays to improve the resolution such as the use of nanodiscs or amphipols proved to be unsuccessful (Appendix Fig S10A). The flexibility of the TssJLM base, which did not allow for it to be resolved, might be due to the absence of other T6SS cytoplasmic components, such as the baseplate. A similar observation was made for the type III secretion system, in which the presence of the cytoplasmic sorting platform orders the IM components (Hu *et al*, 2017). One may hypothesize that this flexibility is essential for the docking of the hexameric baseplate, and to accommodate the five-fold to six-fold symmetry mismatch. One alternative hypothesis is that the disorder at the centre of the base structure is caused by the presence of a lipid bilayer encircled by the TssM and TssL proteins. In the *in vivo* situation, the MC assembles first, before the recruitment of the baseplate (Durand *et al*, 2015; Brunet *et al*, 2015), and hence, one can expect that a lipid bilayer at the entrance of the TssJLM lumen would be present before baseplate docking to prevent the leakage of solutes and proton-motive force.

The high-resolution structure of the EAEC TssJLM MC also revealed new interesting and functional features. First, five additional TssJ subunits, called TssJ', were identified in the tip complex. These TssJ' proteins interact with the TssJ proteins of the inner pillars (TssJ.i). Mutations that interfere with TssJ'-TssJ.i interaction impaired the functional integrity of the MC and hence inactivated the T6SS (Fig 4D-E and Appendix Fig S5). Second, we identified an 11-amino-acid loop in TssM that protrudes from each inner pillar to the centre of the channel, thus creating a constriction

that is observed in the density map (Fig 3B, E and Appendix Fig S3). Each loop is stabilized by the adjacent loop via Asn/Gln pairings (Fig 5D). Such weak interactions could be easily displaced by the VgrG/PAAR spike upon baseplate docking or during firing. Our mutational analyses demonstrate that this constriction is important for TssJLM MC formation and T6SS activity. Periplasmic constrictions are usual features of trans-envelope complexes. The best characterized examples include the OM T2SS and T3SS secretins, and the CsgG curli secretion channel, where one or two periplasmic gates are present to prevent leakage (Appendix Fig S11A-B) (Yan *et al*, 2017; Spagnuolo *et al*, 2010; Goyal *et al*, 2014). While we do not know the role of this constriction in the T6SS, we propose that these loops may stabilize the MC in its closed conformation during the resting state. The cryo-EM structure defined two hinge regions that exhibit a certain degree of flexibility (Fig EV4B,G). These two hinges result in the formation of the two layers of pillars, with the inner layer obstructing the channel. A large conformational change of these pillars is therefore necessary to open the channel for the passage of the tube/spike complex. Interestingly, with an interaction surface of 1540 $Å^2$ (ΔG of 6.1 kcal/mol) the TssM inner pillars contacts are considerably less stable than the contacts within the T2SS secretin (interaction surface of 5353.7 $Å^2$ and ΔG of -52.4 kcal/mol). The displacement of the pillars could be controlled by the flexibility of the hinge regions.

Based on these data, we propose a model in which the T6SS TssJLM MC is assembled in a closed state. In this conformation, five pillars are oriented toward the centre of the complex to close the complex at the outer membrane, and hence to protect the cell from periplasmic leakage or from the entry of toxic compounds. This conformation is further stabilized by the interactions of the TssM protruding loops. The flexibility of the MC cytoplasmic base allows the proper positioning of the TssKFGE-VgrG baseplate, and accommodates the five-to-six symmetry. The docking of the baseplate positions the VgrG/PAAR spike in proximity to the inner membrane. Once in contact with the target cell, a signal transmitted to the baseplate triggers the contraction of the sheath, allowing the passage of the tube/spike complex through the MC. The hinge regions undergo a tectonic conformational change that opens the channel and the tip complex. The MC then returns to the resting, closing state allowing a new cycle to start (Fig 6). This model is still uncomplete and rather speculative. Many aspects of the secretion mechanism by the T6SS remain elusive. Further investigations are therefore needed to provide a complete molecular understanding of this mechanism.

Acknowledgements

We would like to thank Yoann Santin for advice on fluorescent microscopy data recording, treatment and analysis, Erney Ramírez-Aportela for help with map sharpening with LocalDeblur, Marion Decossas-Mendoza and Marie Glavier for help with graphene grids preparation, Laetitia

Daury-Joucla and Olivier Lambert for help with nanodiscs reconstitution, and Tobias Zachs for manual particle picking of subvolumes and for the design of a mask for subtomogram averaging

This work has benefitted from the facilities and expertise of the Biophysical and Structural Chemistry platform (BPCS) at IECB, CNRS UMS3033, Inserm US001, Bordeaux University, in particular we would like to thank Armel Bezault. The authors acknowledge the support and the use of resources of Instruct-ERIC, Diamond light source and Kyle Dent in particular, for the collect of the amphipols-containing sample. ScopeM is acknowledged for instrument access at ETH Zürich, and Ohad Medalia is acknowledged for instrument access at the University of Zürich.

This work was funded by the Centre National de la Recherche Scientifique, the Aix-Marseille Université, and grants from the Agence Nationale de la Recherche (ANR-14-CE14-0006-02, ANR-17-CE11-0039-01) and the Fondation pour la Recherche Médicale (DEQ20180339165) to EC. ED was supported by the INSERM and an EMBO short-term fellowship (ASTF 417 – 2015). YC is supported by a Doctoral school PhD fellowship from the FRM (ECO20160736014). VS is supported by a post-doctoral fellowship from the association Espoir contre la Mucoviscidose. LL was supported by a fourth year PhD fellowship from the FRM (FDT20160435498). MP is funded by the European Research Council, the Swiss National Science Foundation and the Helmut Horten Foundation. RF and CR were supported by IDEX Bordeaux through a “chaire d’excellence” to RF.

Author Contributions

RF, ED, MP and EC conceived the project. CR, RF, ED and MP designed the experiments. YC performed the in vivo studies with the help of VS. RK performed all the cryo-tomography work with help from MP and ED. CR carried out the single particle cryo-EM study with help from RF. RP performed the amino acids interaction analysis and validated the model. LL engineered the *E.coli* mini cells. CR, RK, EC, RF wrote the manuscript with contribution from all of the authors.

Conflict of interest

The authors declare no competing interests.

Figure legends

Figure 1. Subtomogram average of the TssJLM complex *in situ*

A-E Isosurface of the subtomogram average (in pink) with an applied C5 symmetry and 0.69 nm tomographic slices (A-E) at the indicated heights. The average is shown in side view, whereas the slices represent perpendicular slices. The 5 pairs of pillars formed a narrow central channel and separated into 10 arches towards the base (base not visible at the used threshold). The division of the structure into subparts was adapted from (Durand *et al.*, 2015). Subvolumes were extracted from

cryotomograms of ghost cells and FIB-milled intact *E. coli* BL21 cells heterologously expressing TssJLM

A' Slice (0.69 nm) through the non-symmetrized average. Note that the C5 symmetry was visible

Figure 2. Position of TssJLM in the cell envelope

A Slice (9.7 nm) through a cryotomogram of a FIB-milled *E. coli* BL21 cell expressing TssJLM. The average shown in Figure 1 was placed back at the positions and orientations of the individual subvolumes that were used to generate the final average. The zoomed-in area highlights the position of the TssJLM particles within the inner and the outer membrane. Some particles were found in cytoplasmic membrane invaginations, as indicated by white arrows. Scale bar 100 nm

B Isosurface of the final average (orange) merged with the isosurface of a second average (with higher threshold; grey mesh). The panel shows the positioning of TssJLM with respect to both inner (IM) and outer membranes (OM). The distances corresponded to the widest and longest dimensions of the TssJLM complex

C Cryotomographic slices (9.7 nm) showing side views of TssJLM. In these examples, the basal parts of TssJLM (red arrows) could be seen extending into the cytoplasm. Scale bar 10 nm

Figure 3. 3D structure of the TE complex of the T6SS

A Autosharpened Cryo-EM density of the full TE complex composed of TssJ, TssL and TssM. The inner pillars are coloured in green and the outer pillars in blue. The unstructured tip and base are in grey, while the top of the core is in orange

B Vertical cross section of the cryo-EM density. Colouring is according to A. The position of the slices for C-E are indicated. The density of the base appears to be composed of two leaflets, indicated by 2 arrows

C-E Cross sections of A, sliced at positions indicated in B

F Subtracted, masked and unsharpened cryo-EM density of the, mostly unstructured, base

G Locally sharpened cryo-EM density of the subtracted and masked core. Three different views are shown. The colouring is according to A

Figure 4. The TssJ' monomer and its function

A Ribbon diagram and locally sharpened surface representation (transparent= of the three TssJ protomers in orange, labelled TssJ.i, TssJ.o and TssJ' for the inner, outer and additional monomer respectively. In light green and blue are the TssM.i and TssM.o protomers respectively

B Superimposition of the ribbon diagrams of TssM-TssJ heterodimer within the inner (green-orange) and the outer (blue-orange) pillars

C Ribbon diagram of the TssM.o (outer pillar) with the TssJ.o and the TssJ' (orange)

D Fluorescence of prey cells (green) indicating their survival against attacker cells after 4 h. The image of a representative bacterial competition spot is shown on the upper part. The relative fluorescent level (in AU) and the number of recovered E. coli recipient cells are indicated in the lower graph (in log10 of colony forming units (cfu)). The assays were performed from at least three independent cultures, with technical triplicates and a representative technical triplicate is shown. The circles indicate values from technical triplicate, and the average is indicated by the bar

E Time-lapse fluorescence microscopy recordings showing localization and dynamics of the $_{sfGFPT}$ssM fusion protein in the parental (WT) and TssJ mutated strains (TssJ D97K). Individual images were taken every 60 seconds. The corresponding time of each micrograph is indicated in the lower right part of the image. Stable foci in the WT strain and less stable foci in the TssJ D97K strain are respectively indicated by white and blue arrowheads. Scale bars, 1 µm

Figure 5. The TssM protein and the periplasmic gate

A The high-resolution structure of MC complex in different orientations. TssJ is in orange, TssM is in green and blue according to their position as an inner or outer pillar respectively.

B Pseudoatomic model of the N-terminus of TssM.i (green), showing it is composed of 8 helices, coloured in different shades of red and numbered from the C-terminus (1) to the N-terminus (8).

C The pore radius formed by the inner pillar of TssM protomers is highlighted as dots and mapped using HOLE. The atomic model of TssM is coloured according to secondary structure (Helices in pink and strands in brown)**.** A graph shows the pore radius calculated along the centre of the inner pillar of TssMs.

D Ribbon diagram of the region surrounding the periplasmic gate, with the amino acids involved in the formation of the gate in atom form. Gln779 and Asn780-781 from the inner pillars of TssM (green) are labelled in one of the protomers

E Fluorescence of prey cells (green) indicating their survival against attacker cells after 4h. The image of a representative bacterial competition spot is shown on the upper part. The relative fluorescent level (in AU) and the number of recovered *E. coli* recipient cells are indicated in the lower graph (in log10 of colony forming units (cfu)). The assays were performed from at least three independent cultures, with technical triplicates and a representative technical triplicate is shown. The circles indicate values from technical triplicate, and the average is indicated by the bar.

F Fluorescence microscopy recordings showing sfGFPTssM foci in the parental (WT) and TssM mutated strains (TssM Q779C/N780C, TssM Δ777-783). TssM foci containing cells are indicated by arrowheads. Microscopy analyses were performed independently three times, each in technical triplicate, and a representative experiment is shown. Scale bars, 1 µm.

G Fluorescence microscopy recordings showing TssBsfGFP sheath in the parental (WT) and TssM mutated strains (TssM Q779C/N780C, TssM Δ777-783). Fluorescent sheath containing cells are indicated by arrowheads. Microscopy analyses were performed independently three times, each in technical triplicate, and a representative experiment is shown. Scale bars, 1 μm.

Figure 6. Summary of the Type 6 secretion system cycle of action

The T6SS assembly begins first with the recruitment of the membrane complex (MC) in its resting state (1). The MC recruits the baseplate (BP) and the tail tip complex (TTC) is assembled (2). The recently solved structures of the BP (Cherrak *et al*, 2018) and MC (this paper) in the membrane context are shown in the inset. A conformational change leads to the channel opening (3) and release of the toxin onto the VgrG spike by contraction of the TTC (4). Once the secretion has occurred, the TTC is recycled (5) and the MC can return to its resting state (6).

493

494 **Table 1. Bonds between the TssJ and TssM subunits**

Monomer1	Monomer2	Area (Å)	ΔG	Nhb	Nsb
TssM.i	TssM.i-1	1528.78	-5.32	9.2	4.8
TssM.i	TssM.o-1	1168.6	-7.54	4.8	6.2
TssM.i	TssM.o	1126.48	-5.2	5.8	5.4
TssM.o	TssJ'	561.7	-2.38	6.6	0
TssM.i	TssJ.i	546.44	-9	1	0
TssJ.o	TssM.o	528.58	-10.14	5	0
TssJ'	TssJ.i	480.62	-0.82	4.6	5.4
TssM.i	TssJ.o-1	190.26	1.7	4	0
TssJ.i	TssM.o	109.72	-1.14	0.2	0

495

496 **Table 2. Cryo-ET data collection, refinement and validation statistics**

	STA_AvgVol_15000 (EMD- 4561)	STA_AvgVol_23500 (EMD- 4562)
Data collection and processing		
Magnification	42000	42000
Voltage (kV)	300	300
Electron exposure (e–/Å^2)	90	90
Defocus range (μm)	0 to -8	0 to -8
Pixel size (Å)	6.898 (binned once), or 3.45 unbinned	6.898 (binned once), or 3.45 unbinned
Symmetry imposed	C5	C5
Initial particle images (no.)	25276	28463
Final particle images (no.)	15000	23500
Map resolution (Å)	20	
FSC threshold	0.143	
Map resolution range (Å)	NA	
Tomography		
Number of grid points:	928 × 928 × 400	928 × 928 × 400
Voxel size:	13.8 × 13.8× 13.8	13.8 × 13.8× 13.8
Projections	61	61

497

498

499

500 **Table 3. Cryo-EM data collection, refinement and validation statistics**

	TssJLM core complex (EMD-0264) (PDB 6HS7)	TssJLM complex (EMD-0265)	TssJLM C1 complex (EMD-0266)	TssJLM base complex (EMD-0267)
Data collection and processing				
Magnification	120,000X	120,000X	120,000X	120,000X
Voltage (kV)	200	200	200	200
Electron exposure (e–/Å^2)	120	120	120	120
Defocus range (μm)	0.4 to 5 μm	0.4 to 5 μm	0.4 to 5 μm	0.4 to 5 μm
Pixel size (Å)	1.24 Å	1.24 Å	1.24 Å	1.24 Å
Symmetry imposed	C5	C5	C1	C5
Initial particle images (no.)	167,825	167,825	167,825	167,825
Final particle images (no.)	36,828	36,828	36,828	36,828
Map resolution (Å)	4.6Å	4.9Å	7.9Å	17Å
FSC threshold	0.143	0.143	0.143	0.143
Map resolution range (Å)	3.9 and 18 Å	3.8-33 Å	-	-
Tomography				
Number of grid points:				
Voxel size:				
Projections				
Refinement				
Initial model used (PDB code)	4Y7O			
Model resolution (Å)				
FSC threshold	4.6Å			
Model resolution range (Å)				
Map sharpening *B* factor (Å^2)				
Model composition				
Non-hydrogen atoms	52890			
Protein residues	6905			
Ligands	N/A			
B factors (Å^2)				
Protein				
Ligand	N/A			
R.m.s. deviations				
Bond lengths (Å)	0.006			
Bond angles (°)	0.989			
Validation				
MolProbity score	1.92			
Clashscore	6.39			
Poor rotamers (%)	0.04			
Ramachandran plot				
Favored (%)	89.46			
Allowed (%)	10.54			
Disallowed (%)	0			

501

502

Expanded view Figure legends:

Figure EV1. The TssJLM complex exhibits a C5 symmetry in *E. coli* BL21 and in EAEC.

A Slice (13.8 nm) through an engineered BL21 minicell with a diameter of ~450nm. Scale bar 100 nm

B-J Slices showing side views (upper row) and top views (lower row) of TssJLM embedded in the cell envelope of BL21(DE3) (expressing TssJLM) and EAEC cells, as indicated by red arrows. The outer and inner membranes are indicated (OM and IM). Scale bars 10 nm

B Slice (9.7 nm) showing a side view of a TssJLM particle embedded in the cell envelope of a BL21 minicell. The particle spanned the periplasm and resembled an inverted Y letter

C Slice (9.7 nm) showing a top view of a TssJLM particle embedded in the membrane of a BL21 minicell. The particle resembles a 5-branched star

D Slice (9.7 nm) showing a side view of a particle embedded in the cell envelope of a BL21 ghost cell

E Slice (9.7 nm) showing a top view of a particle embedded in the cell envelope of a BL21 ghost cell

F Slice (9.7 nm) showing a side view of a particle embedded in the cell envelope of a FIB-milled BL21 cell.

G Slice (13.8 nm) showing a top view of a particle embedded in the cell envelope of a FIB-milled BL21 cell

H Slice (9.9 nm) showing a side view of a particle embedded in the cell envelope of an EAEC cell in which TssJLM was heterologously overexpressed

I Slice (9.9 nm) showing a side view of a particle embedded in the cell envelope of a wild type EAEC cell

J Slice (9.9 nm) through the distorted periplasm of an EAEC in which TssJLM was heterologously overexpressed. The particles seen in side view were detached from the OM but still attached to the periplasmic side of the IM

Figure EV2. The cryo-EM reconstruction of the core of the membrane complex (MC)

A 2D classes of the subtracted SPA cryo-EM density corresponding to the core of the MC

B FSC curve of the core complex as calculated using postprocess

C 3D representation of the core 3d reconstruction coloured according to the local resolution. Two views are shown

D Fitting of 10 TssM-TssJ pseudoatomic models from the crystal structure (4Y7O) in the core cryo-EM density locally sharpened. The cryo-EM density was coloured according to the fitted structure. The five additional densities are highlighted by arrows pointing at them. Two views of the complexes are shown. In orange is the TssJ, in blue the beta sheet-rich region and in cyan the alpha helical domain

E Transparent representation of the cryo-EM density in which the third TssJ was fitted (ribbon diagram in orange). The colouring follows that in D

F Representative cryo-EM density, corresponding to the TssJ' sequence 27-33, with the fitted pseudoatomic model in stick form

Figure EV3. The TssJ-TssM assembly

A Schematic diagram of the TssM-TssJ assembly, labelled according to the nomenclature used throughout this paper.

B Superimposition of two slices through the MC complex corresponding to TssJ in orange and TssM in light blue, mimicking the diagram A.

C TssJ.o-TssJ' interface (in orange) with the two residues involved in the interaction as an atom diagram and labelled

Figure EV4. The TssM pseudoatomic model

A Comparison between the TssM from the PDB (4Y7O) in cyan and the refined TssM on the cryo-EM density in orange

B Comparison of the pseudoatomic model of TssM in the internal (green) and in the external (blue) pillars

C Interaction interfaces between the internal TssM.a and the external TssM.A within the complex

D Interaction interfaces between the internal pillars TssM.a and TssM.a^{+1}. The two pillars are twisted at 76˚ with respect to one another

E Interaction interfaces between the internal pillar TssM.a and the external TssM.A^{+1}. The two pillars are twisted at 68˚ with respect to one another

F Weak C-terminal density of TssM (1109-1129) in pink

G The unsharpened density map of the whole complex at a contour level of 0.0055. The TssM foot domain (in blue) between amino acids 382 and 570 predicted structure by RaptorX fits into the density. The two feet converge upon arriving at the membrane level. The rest of the pseudoatomic model of TssM is in pink

Expanded view Movie legends

Movie 1. Movie of a cryotomogram of a FIB-milled E. coli BL21(DE3) cell expressing TssJLM. The average was placed back at the positions and orientations of the individual subvolumes that were used to generate the final average. The movie shows the position of TssJLM within the cell envelope. Some particles were found in cytoplasmic membrane invaginations

Movie 2. Movie of a cryotomogram of an E. coli BL21 ghost cell expressing TssJLM. The average was placed back in the tomogram at the individual positions and orientations that were used to generate the final average

Movie 3. The first part shows the cryotomogram of a FIB-milled E. coli BL21(DE3) cell expressing TssJLM (same cell as in Movie 1) in which the average was placed back at the positions and orientations of the individual subvolumes that were used to generate the final average. The second part shows a morph between the in situ structure and the high resolution cryoEM structure. The third part shows the high resolution structure with the pseudoatomic model, focusing on the position of the periplasmic gate (first pause) and the periplasmic channel (second pause). The last part replaces the cryoEM structure in the cell envelope at the same position as the in situ structure at the beginning of the movie

589 **Materials and methods**

590

591 **Strains and media**

592 Strains used in this study are listed in Appendix Table S1. The *E. coli* K-12 W3110 bearing the pUA66-
593 *rrnB* vector (Kan^R and GFP^+, (Zaslaver *et al*, 2006)) was used as recipient for antibacterial competition
594 assays. Strains were routinely grown in lysogeny broth (LB) rich medium or in Sci-1-inducing medium
595 (SIM; M9 minimal medium, glycerol 0.2%, vitamin B1 1 $\mu g.mL^{-1}$, casaminoacids 100 $mg.mL^{-1}$, LB 10%,
596 supplemented or not with bactoagar 1.5%) (Brunet *et al*, 2011) with shaking at 37°C.

597

598 **Strain construction**

599 *tssM* and *tssJ* point mutations were engineered at the native locus on the chromosome by allelic
600 replacement using the pKO3 suicide vector (Link *et al*, 1997) into the enteroaggregative *E. coli* 17-2
601 strain. Briefly, 17-2 WT strain was transformed with a pKO3 plasmid in which a fragment of the *tssM*
602 or *tssJ* gene carrying the point mutations has been cloned (see below). Insertion of the plasmid into
603 the chromosome was selected on chloramphenicol plates at 42°C. Plasmid sequences removal was
604 then selected on 5% sucrose plates without antibiotic and *tssM* point mutation recombinant strains
605 were screened by PCR and confirmed by DNA sequencing (Eurofins,MWG). Chromosomal fluorescent
606 reporter insertions into the enteroaggregative *E. coli* 17-2 strain mutated in *tssM* or *tssJ* was
607 achieved by using a modified one-step inactivation procedure (Datsenko & Wanner, 2000) as
608 previously described (Aschtgen *et al*, 2008b) using plasmid pKOBEG (Chaveroche *et al*, 2000). Briefly,
609 a kanamycin cassette was amplified from plasmid pKD4 using oligonucleotide pairs carrying 5' 50-
610 nucleotide extensions homologous to regions adjacent to the gene to be deleted. After
611 electroporation of 600 ng of column-purified PCR product, kanamycin-resistant clones were selected
612 and verified by colony-PCR. The kanamycin cassette, inserted at the gene locus on the bacterial
613 chromosome, was then excised using plasmid pCP20, leaving an FRT scars. Gene deletions were
614 confirmed by colony-PCR and sequencing.

615

616 **Fluorescence microscopy, image treatment and analyses**

617 Fluorescence microscopy experiments were performed as described (Brunet *et al*, 2013; Zoued *et al*,
618 2013). Briefly, cells were grown overnight in LB medium and diluted to A_{600nm} ~ 0.04 in SIM.
619 Exponentially growing cells (A_{600nm} ~ 0.8–1) were harvested, washed in phosphate-buffered saline
620 buffer (PBS), resuspended in PBS to A_{600nm} ~ 50, spotted on a 1.5% agarose pad and covered with a
621 cover slip. Fluorescence micrographs were captured using AxioImager M2 microscope (Zeiss)
622 equipped with an OrcaR2 digital camera (Hamamatsu). For time lapse fluorescence microscopy,
623 images were recorded with a Nikon Eclipse Ti microscope equipped with an Orcaflash 4.0 LT digital

624 camera (Hamamatsu) and a perfect focus system (PFS) to automatically maintain focus so that the
625 point of interest within a specimen is always kept in sharp focus at all times despite mechanical or
626 thermal perturbations. Fluorescence images were acquired with a minimal exposure time to reduce
627 bleaching and phototoxicity effects, typically 200 ms for TssB-sfGFP and 300 ms for sfGFP-TssM. For
628 image treatment, noise and background were reduced using the 'Subtract Background' (20 pixels
629 Rolling Ball) and Band plugins of imageJ (Schneider *et al*, 2012). The sfGFP foci were automatically
630 detected using the microbeJ plugin (Ducret *et al*, 2016). Floating bars representing the number of
631 detected foci for each strain were made using GraphPad (https://www.graphpad.com). Microscopy
632 analyses were performed at least three times, each in technical triplicate, and a representative
633 experiment is shown.
634
635 **Interbacterial competition assay**
636 The antibacterial growth competition assay was performed as previously described (Flaugnatti *et al*,
637 2016). Wild-type *E. coli* K-12 strain W3110 bearing the pUA66-*rrnB* plasmid (conferring kanamycin
638 resistance and constitutive GFP fluorescence (*gfp* gene under the control of the ribosomal *rrnB*
639 promoter, (Gueguen & Cascales, 2013) was used as recipient. Attacker and recipient cells were
640 grown for 16 h in LB medium, diluted in SIM to allow maximal expression of the *sci-1* gene cluster
641 (Brunet *et al*, 2011). Once the culture reached A_{600nm}~ 0.8, cells were harvested and normalized to
642 A_{600nm} = 0.5 in SIM. Attacker and recipient cells were mixed to a 4:1 ratio and 15-µl drops of the
643 mixture were spotted in triplicate onto a pre-warmed dry SIM agar plate. After incubation for 4 h at
644 37°C, the bacterial spots were resuspended in LB and bacterial suspensions were normalized to
645 A_{600nm} = 0.5. For the enumeration of viable prey cells, bacterial suspensions were serially diluted and
646 spotted onto kanamycin LB plates. The assays were performed from at least three independent
647 cultures, with technical triplicates and a representative technical triplicate is shown.
648
649 **Protein preparation**
650 The expression and purification of the TssJLM complex was carried out as previously described
651 (Durand *et al*, 2015), with the exception that the cryo-EM grids were prepared immediately after the
652 HisTrap Elution. For the amphipole-containing sample, the Strep-Trap elution was incubated with
653 amphipoles A8-35 (Anatrace, USA) and subjected to gel filtration on a superpose 6 (GE Healthcare,
654 UK) to remove residual detergent.
655
656 **Cryo-EM grids preparation and data acquisition**
657 C-flat ™ (CF-2/1-2C) grids were coated with graphene oxide as previously described (Martin *et al*,
658 2016). 3.5 µl of the sample at 0.2 mg.mL-1, was loaded on the copper side and then blotted on the

same side for 2s in a Leica EM GP at 80% humidity and 4 ˚C, before being plunge frozen in liquid ethane (-184˚C). Micrographs (Appendix Fig S2B) at a nominal magnification of 120,000 X were collected in a Talos Arctica electron microscope equipped with a Falcon 3EC camera (Thermo Fisher, Waltham, MA, USA) in linear mode and with a pixel size of 1.24 Å. Dose-fractionated movie frames 20/micrograph were acquired for 1 s with a total electron flux of 120 e/Å/s. The defocus range chosen for the automatic collect was 0.7 to 2 µm, which resulted in an actual range between 0.4 to 5 µm.

For the amphipoles-containing MC collection, 3019 movies composed of 25 frames at a defocus range between 0.7 and 2µm, were collected at 1.38Å pixel size with a 5s exposure time and 15 e/pix/s exposure rate at the Krios 2 at the Diamond eBIC facility.

Cryo-EM image processing

The 16,000 movies collected were aligned using MotionCor2, with dose weighting (6 e-/Å^2/frame) and with 5X5 patches applied (Zheng *et al*, 2017). gCTF was used to estimate the CTF parameters (Zhang, 2016) and low quality images were discarded. Relion 2.1 (Scheres, 2012) autopicked 227,527 particles and after several rounds of 2D classification in cryosparc (Punjani *et al*, 2017) and a heterogeneous *ab initio* reconstruction (2 classes), 37,435 particles were converted using the script csparc2star.py (Asarnow, 2016) and selected for a final 2D classification in relion 2.1 (Appendix Fig S2C), of which 36,828 particles were selected. An initial unmasked refinement using the *ab initio* model from crysoparc, gave us a resolution of 7.6 Å with 5-fold applied symmetry and a soft mask of 450 Å. This refined structure was used to do a movie refinement with all the frames and a polishing step with RELION2.1. The final masked refinement of the full structure gave a final resolution of 4.9 Å with a C5 symmetry applied, and 7.9 Å with no symmetry applied (Appendix Fig S2E, I), The disordered tip and base were subtracted and a masked refinement around the core structure yielded a final resolution of 4.6 Å (Fig EV2B). The base focused refinement was also performed on subtracted particles, without the tip and the core regions, to a resolution of 17Å (Appendix Fig S4F). The resolution for all densities except the base, was calculated by masked postprocessing according to the “gold standard” method using 0.143 as the FSC value cut-off, or 0.5 for the low resolution reconstruction (Rosenthal & Henderson, 2003) and the local resolution of the core was calculated by relion 2.1 (Fig EV2C).

For figures and to build *de novo* pseudoatomic models in Coot (Emsley *et al*, 2010), the cryo-EM density was initially sharpened using phenix.autosharpen (Terwilliger *et al*, 2018) and later with LocalDeblur (Ramírez-aportela *et al*, 2018). Fitting of density, correlation calculations, molecular graphics and analyses were performed on UCSF Chimera (Pettersen *et al*, 2004). For the amphipoles dataset, 2D classes were calculated from a total of 8637 particles (Appendix Fig S10A).

694

695 **Model building**

696 Model building proceeded by fitting the PDB 4Y7O (Durand *et al*, 2015) into the density 2 times for
697 each pillar, with the cross correlation being calculated using Chimera (Pettersen *et al*, 2004)(Fig
698 EV2D). To complete the structure of TssM beyond the known region, which spanned aa. 869-1129,
699 we used the *de novo* tracing strategy that we introduced in an earlier work (Cherrak *et al*, 2018).
700 Briefly, we iterated between manual model building and structural refinement on Coot (Emsley *et al*,
701 2010) using bulky sidechains and secondary structure predictions obtained by Phyre2 (Kelley *et al*,
702 2015) as guides, and sequence-structure registration based on contact prediction obtained by
703 RaptorX (Källberg *et al*, 2012). The map of the predicted contacts was aligned with those of the built
704 PDB, the algorithm introduced by the MapAlign software (Ovchinnikov *et al*, 2017). Where
705 discrepancies were observed, the register was modified to fit the predicted contact maps (Appendix
706 Fig S6). The model was eventually refined using one round of rosetta.refine (Wang *et al*, 2016) and
707 phenix.real_space_refine (Afonine *et al*, 2018). This procedure allowed us to extend the structure of
708 TssM to the fragment spanning residues 579 to 869, and to produce a model of the fragment
709 between amino acids 390 and 550.

710

711

712 **Validation of the data**

713 The model was validated as in the protocol in Refmac5 (Murshudov *et al*, 2011). The FSC map to
714 model was calculated with the sharpened map (FSC_{sum}). The model was shaken by 0.5 Å and the FSC
715 map to model was calculated with one Half map (FSC_{work}). This refined model was then used to
716 calculate the FSC map to model with the other Half map (FSC_{free}) (Appendix Fig S12A).
717 The cross correlation between each amino acid in the model and map was also calculated with
718 phenix.real_space_refine (Afonine *et al*, 2018) (Appendix Fig S12B) and the Molprobity score (Chen
719 *et al*, 2010). was obtained from the online server (Table 3) Pore radius calculations were carried out
720 using the HOLE (Smart et al, 1996) plugin in Coot and the protein interfaces were analysed with PISA
721 (Krissinel & Henrick, 2007).

722

723 **Strains, media and chemicals**

724 The strains, plasmids and nucleotides used in this study are listed in Appendix Tables S1 and S2. For
725 the cryo-ET studies, *E. coli* K-12 BL21(DE3) and enteroaggregative *E. coli* EAEC strain 17-2 were used
726 for protein overexpression before plunge freezing. Strains were routinely grown in LB-Miller or in Sci-
727 1-inducing medium (SIM; M9 minimal medium, glycerol 0.2%, vitamin B1 1 mg ml^{-1}, casaminoacids
728 100 mg ml^{-1}, LB 10%, supplemented or not with bactoagar 1.5%) (Brunet *et al*, 2011) with shaking at

37°C. Plasmids were maintained by the addition of ampicillin (100 mg ml^{-1} for E. coli K-12, 200 mg ml^{-1} for EAEC), kanamycin (50 mg ml^{-1}) or chloramphenicol (30 mg ml^{-1}). Expression of genes from pRSF (in BL21) and pBAD33 (in EAEC) vectors was induced for 2-3h with 1 mM of isopropyl-b-D-thio-galactopyranoside (IPTG) or 0.3% L-arabinose, respectively.

Preparation of frozen-hydrated specimens

Plunge freezing was performed according to (Weiss *et al*, 2017). *E. coli* BL21 or EAEC cells were concentrated by centrifugation to an OD_{600} of 3 - 20 and then mixed with protein A – 10 nm gold conjugate (Cytodiagnostics Inc.). The higher concentrations of cells were used when preparing grids for cryo-focused ion beam (cryo-FIB) milling to form "bacterial lawns" of several layers of bacteria on top of each other. Bacterial lawns were found to be more amenable to cryo-FIB milling then individual cells. A 3 μL droplet of the sample was applied to a carbon-coated EM copper grid (R2/1, Quantifoil) that had been previously glow-discharged for 90 s at -25 mA using a Pelco easiGlow™ (Ted Pella, Inc.). The grid was plunge-frozen in liquid ethane-propane (37 %/63 %) using a Mark IV Vitrobot (Thermo Fisher Scientific). The forceps were mounted in the Vitrobot (27°C, humidity 95%) and the grid was blotted from both sides or only from the backside by installing a Teflon sheet (instead of a filter paper) on the front blotting pad. Grids were stored in liquid nitrogen.

Cryo-focused ion beam milling

Cryo-focused ion beam (cryo-FIB) milling was used to prepare samples of plunge-frozen cells that could then be imaged by electron cryotomography (Marko *et al*, 2007). Our cryo-FIB milling workflow has been detailed in (Medeiros *et al*, 2018b). Frozen grids with lawns of *E. coli* BL21 cells overexpressing TssJLM were clipped into modified Autogrids provided by J. Plitzko or a commercial prototype provided by Thermo Fisher. We then transferred the grids into the liquid nitrogen bath of a loading station (Leica Microsystems) and clamped them onto a "40° pre-tilted TEM grid holder" (Leica Microsystems). The holder with grids was shuttled from the loading station to the dual beam instrument using the VCT100 transfer system (Leica Microsystems). The holder was mounted on a custom-built cryo-stage in a Helios NanoLab600i dual beam FIB/SEM instrument (FEI). The stage temperature was maintained below -154°C during loading, milling and unloading procedures. Grid quality was checked by scanning EM (SEM) imaging (5 kV, 21 pA). The samples were then coated with a Platinum (Pt) precursor gas using the Gas Injector System. We adapted a "cold deposition" technique that was published previously (Hayles *et al*, 2007) (needle distance to target of 8 mm, temperature of the precursor gas of 27 °C, and open valve time of 5 s). Lamellae were milled in several steps. We first targeted two rectangular regions to generate a lamella with ~2 μm thickness with the ion beam set to 30 kV and ~400 pA. The current of the ion beam was then gradually reduced

until the lamella reached a nominal thickness of 150-400 nm (ion beam set to ~25 pA). Up to 6 lamellae were milled per grid. After documentation of the lamellae by SEM imaging, the holder was brought back to the loading station using the VCT100 transfer system. The grids were unloaded and stored in liquid nitrogen.

Electron cryomicroscopy and electron cryotomography

E. coli BL21 and EAEC cells (overexpressing TssJLM where indicated), cryo-FIB-processed *E. coli* BL21 cells overexpressing TssJLM, and purified TssJLM samples were examined by electron cryotomography (cryoET). Images were recorded on a Tecnai Polara TEM (Thermo Fisher Scientific) equipped with post-column GIF 2002 imaging filter and K2 Summit direct electron detector (Gatan), or on a Titan Krios TEM (Thermo Fisher Scientific) equipped with a Quantum LS imaging filter and K2 Summit (Gatan). Both microscopes were operated at 300kV and the imaging filters with a 20 eV slit width. The pixel size at the specimen level ranged from 4.93 Å to 4.05 Å. The latter pixel-sized was used for the sub-tomogram average. Tilt series covered an angular range from -60° to +60° with 2° (lamellae, sheath preparations) increments and -10 to -6 μm defocus, or in focus (0 μm defocus) when the data was collected on the Titan Krios with a Volta phase plate (Thermo Fisher Scientific) (Danev & Baumeister, 2016). The total dose of a tilt series was 60-100 $e^-/Å^2$. Tilt series and 2D projection images were acquired automatically using UCSF Tomo (Zheng *et al*, 2007) on the Tecnai Polara and SerialEM (Mastronarde, 2005) on the Titan Krios. Three-dimensional reconstructions and segmentations were generated using the IMOD program suite (Kremer *et al*, 1996a). Table 2 summarises the data collection, refinement and validation statistics.

Sub-tomogram averaging

Tomograms used for subtomogram averaging were not CTF-corrected, as most of the particles were extracted from tomograms collected in focus with the Volta phase plate. Individual particles were identified visually in tomograms as 5-branched stars shapes in top and bottom views and as inverted-Y shapes in side views and their longitudinal axes were manually modelled with open contours in 3dmod (Kremer *et al*, 1996b). The manual particle picking and first round of sub-tomogram averaging were performed with the PEET software package on tomograms that were binned by 4 (1k reconstructions). Model points, the initial motive list, and the particle rotation axes were generated using the stalkInit program from the PEET package (Nicastro, 2006). This approach allowed the definition of each structure's longitudinal axis as the particle y-axis. 28474 individual particles extracted from cryotomograms of *E. coli* BL21 ghost and FIB-milled cells were averaged using PEET with a box size of 44 pixels in x and z, and 72 pixels in y for the final step on data binned by 2 (2k reconstruction, final pixel size 8.1 Å). A random particle was chosen as a first reference.

Missing wedge compensation was activated. The final motive lists obtained after this initial average performed on tomograms that were binned by 4 were then translated and used to perform a new round of sub-tomogram averaging on tomograms that were binned by 2 (2k reconstructions). From individual particles and after analysing the resulting average, C_5 symmetry was imposed. The Fourier shell correlation curves were calculated in PEET to estimate resolution. A cylindrical mask centred on the structure's longitudinal axis was applied to the volumes using imodmop (IMOD package) in order to mask neighbouring structures and the membranes during averaging. 3dmod (IMOD package) and UCSF Chimera (Pettersen *et al*, 2004) were used for visualization of the averages. 3dmod was used for generating all the movies, except for the morph and the atomic model visualization in Movie 3 that were generated in UCSF Chimera.

Data availability

The cryo-EM structure of the TssJLM core, full complex (C5 and C1 symmetry) and base were deposited in the EMDB under ID codes EMD-0264, 0265, 0266 and 0267 respectively. The TssJLM core atomic model were deposited in the PDB under ID code PDB 6HS7. The cryo-tomography maps were deposited under ID codes EMD-4561 and 4562. Raw cryo-EM data are available on request.

References

Afonine P V., Poon BK, Read RJ, Sobolev O V., Terwilliger TC, Urzhumtsev A & Adams PD (2018) Real-space refinement in PHENIX for cryo-EM and crystallography. *Acta Crystallogr. Sect. D Struct. Biol.* **74:** 531–544

Asarnow D (2016) Pyem. *GitHub* Available at: https://github.com/asarnow/pyem

Aschtgen M-S, Bernard CS, De Bentzmann S, Lloubes R & Cascales E (2008a) SciN Is an Outer Membrane Lipoprotein Required for Type VI Secretion in Enteroaggregative Escherichia coli. *J. Bacteriol.* **190:** 7523–7531

Aschtgen M-S, Bernard CS, De Bentzmann S, Lloubes R & Cascales E (2008b) SciN Is an Outer Membrane Lipoprotein Required for Type VI Secretion in Enteroaggregative Escherichia coli. *J. Bacteriol.* **190:** 7523–7531

Aschtgen MS, Zoued A, Lloubès R, Journet L & Cascales E (2012) The C-tail anchored TssL subunit, an essential protein of the enteroaggregative Escherichia coli Sci-1 Type VI secretion system, is inserted by YidC. *Microbiologyopen*

Basler M, Pilhofer M, Henderson GP, Jensen GJ & Mekalanos JJ (2012) Type VI secretion requires a dynamic contractile phage tail-like structure. *Nature* **483:** 182–186

Boyer F, Fichant G, Berthod J, Vandenbrouck Y & Attree I (2009) Dissecting the bacterial type VI secretion system by a genome wide in silico analysis: what can be learned from available microbial genomic resources? *BMC Genomics* **10:** 104

Brunet YR, Bernard CS, Gavioli M, Lloubès R & Cascales E (2011) An Epigenetic Switch Involving Overlapping Fur and DNA Methylation Optimizes Expression of a Type VI Secretion Gene Cluster. *PLoS Genet.* **7:** e1002205

Brunet YR, Espinosa L, Harchouni S, Mignot T & Cascales E (2013) Imaging Type VI Secretion-Mediated Bacterial Killing. *Cell Rep.* **3:** 36–41

Brunet YR, Henin J, Celia H & Cascales E (2014) Type VI secretion and bacteriophage tail tubes share a common assembly pathway. *EMBO Rep.* **15:** 315–321

Brunet YR, Zoued A, Boyer F, Douzi B & Cascales E (2015) The Type VI Secretion TssEFGK-VgrG Phage-Like Baseplate Is Recruited to the TssJLM Membrane Complex via Multiple Contacts and Serves As Assembly Platform for Tail Tube/Sheath Polymerization. *PLOS Genet.* **11:** e1005545

Celniker G, Nimrod G, Ashkenazy H, Glaser F, Martz E, Mayrose I, Pupko T & Ben-Tal N (2013) ConSurf: Using Evolutionary Data to Raise Testable Hypotheses about Protein Function. *Isr. J. Chem.* **53:** 199–206

Chang JH & Kim Y-G (2015) Crystal structure of the bacterial type VI secretion system component TssL from Vibrio cholerae. *J. Microbiol.*

Chang Y, Rettberg LA, Ortega DR & Jensen GJ (2017) *In vivo* structures of an intact type VI secretion

system revealed by electron cryotomography. *EMBO Rep.* **18:** 1090–1099

Chaveroche MK, Ghigo JM & d'Enfert C (2000) A rapid method for efficient gene replacement in the filamentous fungus Aspergillus nidulans. *Nucleic Acids Res.* **28:** E97

Chen VB, Arendall WB, Headd JJ, Keedy DA, Immormino RM, Kapral GJ, Murray LW, Richardson JS & Richardson DC (2010) MolProbity : all-atom structure validation for macromolecular crystallography. *Acta Crystallogr. Sect. D Biol. Crystallogr.* **66:** 12–21

Cherrak Y, Rapisarda C, Pellarin R, Bouvier G, Bardiaux B, Allain F, Malosse C, Rey M, Chamot-Rooke J, Cascales E, Fronzes R & Durand E (2018) Biogenesis and structure of a type VI secretion baseplate. *Nat. Microbiol.* **3:** 1404–1416

Clemens DL, Ge P, Lee B-Y, Horwitz MA & Zhou ZH (2015) Atomic Structure of T6SS Reveals Interlaced Array Essential to Function. *Cell* **160:** 940–951

Danev R & Baumeister W (2016) Cryo-EM single particle analysis with the Volta phase plate. *Elife* **5:**

Datsenko KA & Wanner BL (2000) One-step inactivation of chromosomal genes in Escherichia coli K-12 using PCR products. *Proc. Natl. Acad. Sci.* **97:** 6640–6645

Ducret A, Quardokus EM & Brun Y V. (2016) MicrobeJ, a tool for high throughput bacterial cell detection and quantitative analysis. *Nat. Microbiol.* **1:** 16077

Durand E, Nguyen VS, Zoued A, Logger L, Péhau-Arnaudet G, Aschtgen M-S, Spinelli S, Desmyter A, Bardiaux B, Dujeancourt A, Roussel A, Cambillau C, Cascales E & Fronzes R (2015) Biogenesis and structure of a type VI secretion membrane core complex. *Nature* **523:** 555–560

Durand E, Zoued A, Spinelli S, Watson PJH, Aschtgen M-S, Journet L, Cambillau C & Cascales E (2012) Structural characterization and oligomerization of the TssL protein, a component shared by bacterial type VI and type IVb secretion systems. *J. Biol. Chem.* **287:** 14157–68

Emsley P, Lohkamp B, Scott WG & Cowtan K (2010) Features and development of Coot. *Acta Crystallogr. Sect. D Biol. Crystallogr.* **66:** 486–501

Felisberto-Rodrigues C, Durand E, Aschtgen M-S, Blangy S, Ortiz-Lombardia M, Douzi B, Cambillau C & Cascales E (2011) Towards a structural comprehension of bacterial type VI secretion systems: characterization of the TssJ-TssM complex of an Escherichia coli pathovar. *PLoS Pathog.* **7:** e1002386

Flaugnatti N, Le TTH, Canaan S, Aschtgen M-S, Nguyen VS, Blangy S, Kellenberger C, Roussel A, Cambillau C, Cascales E & Journet L (2016) A phospholipase A 1 antibacterial Type VI secretion effector interacts directly with the C-terminal domain of the VgrG spike protein for delivery. *Mol. Microbiol.* **99:** 1099–1118

Fu X, Himes BA, Ke D, Rice WJ, Ning J & Zhang P (2014) Controlled bacterial lysis for electron tomography of native cell membranes. *Structure* **22:** 1875–1882

Goyal P, Krasteva P V, Van Gerven N, Gubellini F, Van den Broeck I, Troupiotis-Tsaïlaki A, Jonckheere

W, Péhau-Arnaudet G, Pinkner JS, Chapman MR, Hultgren SJ, Howorka S, Fronzes R & Remaut H (2014) Structural and mechanistic insights into the bacterial amyloid secretion channel CsgG. *Nature* **516:** 250–3

Gueguen E & Cascales E (2013) Promoter Swapping Unveils the Role of the Citrobacter rodentium CTS1 Type VI Secretion System in Interbacterial Competition. *Appl. Environ. Microbiol.* **79:** 32–38

Hachani A, Wood TE & Filloux A (2016) Type VI secretion and anti-host effectors. *Curr. Opin. Microbiol.* **29:** 81–93

Hayles MF, Stokes DJ, Phifer D & Findlay KC (2007) A technique for improved focused ion beam milling of cryo-prepared life science specimens. *J. Microsc.* **226:** 263–9

Hu B, Lara-Tejero M, Kong Q, Galán JE & Liu J (2017) In Situ Molecular Architecture of the Salmonella Type III Secretion Machine. *Cell* **168:** 1065–1074.e10

Jo S, Kim T & Im W (2007) Automated builder and database of protein/membrane complexes for molecular dynamics simulations. *PLoS One* **2:**

Källberg M, Wang H, Wang S, Peng J, Wang Z, Lu H & Xu J (2012) Template-based protein structure modeling using the RaptorX web server. *Nat. Protoc.* **7:** 1511–1522

Kelley LA, Mezulis S, Yates CM, Wass MN & Sternberg MJE (2015) The Phyre2 web portal for protein modeling, prediction and analysis. *Nat. Protoc.* **10:** 845–858

Kremer JR, Mastronarde DN & McIntosh JR (1996a) Computer Visualization of Three-Dimensional Image Data Using IMOD. *J. Struct. Biol.* **116:** 71–76

Kremer JR, Mastronarde DN & McIntosh JR (1996b) Computer Visualization of Three-Dimensional Image Data Using IMOD. *J. Struct. Biol.* **116:** 71–76

Krissinel E & Henrick K (2007) Inference of Macromolecular Assemblies from Crystalline State. *J. Mol. Biol.* **372:** 774–797

Kudryashev M, Wang RY-R, Brackmann M, Scherer S, Maier T, Baker D, DiMaio F, Stahlberg H, Egelman EH & Basler M (2015) Structure of the Type VI Secretion System Contractile Sheath. *Cell* **160:** 952–962

Link AJ, Phillips D & Church GM (1997) Methods for generating precise deletions and insertions in the genome of wild-type Escherichia coli: application to open reading frame characterization. *J. Bacteriol.* **179:** 6228–6237

Logger L, Aschtgen M-S, Guérin M, Cascales E & Durand E (2016) Molecular Dissection of the Interface between the Type VI Secretion TssM Cytoplasmic Domain and the TssG Baseplate Component. *J. Mol. Biol.* **428:** 4424–4437

Ma L-S, Lin J-S & Lai E-M (2009) An IcmF Family Protein, ImpLM, Is an Integral Inner Membrane Protein Interacting with ImpKL, and Its Walker A Motif Is Required for Type VI Secretion System-

921 Mediated Hcp Secretion in Agrobacterium tumefaciens. *J. Bacteriol.* **191:** 4316–4329
922 Marko M, Hsieh C, Schalek R, Frank J & Mannella C (2007) Focused-ion-beam thinning of frozen-
923 hydrated biological specimens for cryo-electron microscopy. *Nat. Methods* **4:** 215–217
924 Martin TG, Boland A, Fitzpatrick AWP & Scheres SHW (2016) Graphene Oxide Grid Preparation.
925 Mastronarde DN (2005) Automated electron microscope tomography using robust prediction of
926 specimen movements. *J. Struct. Biol.* **152:** 36–51
927 Medeiros JM, Böck D & Pilhofer M (2018a) Imaging bacteria inside their host by cryo-focused ion
928 beam milling and electron cryotomography. *Curr. Opin. Microbiol.* **43:** 62–68
929 Medeiros JM, Böck D, Weiss GL, Kooger R, Wepf RA & Pilhofer M (2018b) Robust workflow and
930 instrumentation for cryo-focused ion beam milling of samples for electron cryotomography.
931 *Ultramicroscopy* **190:** 1–11
932 Mougous JD, Cuff ME, Raunser S, Shen A, Zhou M, Gifford CA, Goodman AL, Joachimiak G, Ordoñez
933 CL, Lory S, Walz T, Joachimiak A & Mekalanos JJ (2006) A virulence locus of Pseudomonas
934 aeruginosa encodes a protein secretion apparatus. *Science* **312:** 1526–30
935 Murshudov GN, Skubák P, Lebedev AA, Pannu NS, Steiner RA, Nicholls RA, Winn MD, Long F & Vagin
936 AA (2011) REFMAC 5 for the refinement of macromolecular crystal structures. *Acta Crystallogr.*
937 *Sect. D Biol. Crystallogr.* **67:** 355–367
938 Nazarov S, Schneider JP, Brackmann M, Goldie KN, Stahlberg H & Basler M (2018) Cryo-EM
939 reconstruction of Type VI secretion system baseplate and sheath distal end. *EMBO J.* **37:**
940 e97103
941 Nicastro D (2006) The Molecular Architecture of Axonemes Revealed by Cryoelectron Tomography.
942 *Science (80-.).* **313:** 944–948
943 Ovchinnikov S, Park H, Varghese N, Huang P-S, Pavlopoulos GA, Kim DE, Kamisetty H, Kyrpides NC &
944 Baker D (2017) Protein structure determination using metagenome sequence data. *Science (80-.*
945 *).* **355:** 294–298
946 Pettersen EF, Goddard TD, Huang CC, Couch GS, Greenblatt DM, Meng EC & Ferrin TE (2004) UCSF
947 Chimera--a visualization system for exploratory research and analysis. *J. Comput. Chem.* **25:**
948 1605–12
949 Punjani A, Rubinstein JL, Fleet DJ & Brubaker MA (2017) cryoSPARC: algorithms for rapid
950 unsupervised cryo-EM structure determination. *Nat. Methods* **14:** 290–296
951 Quentin D, Ahmad S, Shanthamoorthy P, Mougous JD, Whitney JC & Raunser S (2018) Mechanism of
952 loading and translocation of type VI secretion system effector Tse6. *Nat. Microbiol.* **3:** 1142–
953 1152
954 Ramírez-aportela E, Vilas JL, Melero R & Conesa P (2018) Automatic local resolution-based
955 sharpening of cryo-EM maps. *bioRxiv***:** 1–21

Rao VA, Shepherd SM, English G, Coulthurst SJ & Hunter WN (2011) The structure of Serratia marcescens Lip, a membrane-bound component of the type VI secretion system. *Acta Crystallogr. Sect. D Biol. Crystallogr.*

Renault MG, Zamarreno Beas J, Douzi B, Chabalier M, Zoued A, Brunet YR, Cambillau C, Journet L & Cascales E (2018) The gp27-like Hub of VgrG Serves as Adaptor to Promote Hcp Tube Assembly. *J. Mol. Biol.*

Robb CS, Assmus M, Nano FE & Boraston AB (2013) Structure of the T6SS lipoprotein TssJ1 from Pseudomonas aeruginosa. *Acta Crystallogr. Sect. F. Struct. Biol. Cryst. Commun.* **69:** 607–10

Robb CS, Nano FE & Boraston AB (2012) The structure of the conserved type six secretion protein TssL (DotU) from Francisella novicida. *J. Mol. Biol.*

Rosenthal PB & Henderson R (2003) Optimal Determination of Particle Orientation, Absolute Hand, and Contrast Loss in Single-particle Electron Cryomicroscopy. *J. Mol. Biol.* **333:** 721–745

Russell AB, Hood RD, Bui NK, LeRoux M, Vollmer W & Mougous JD (2011) Type VI secretion delivers bacteriolytic effectors to target cells. *Nature* **475:** 343–347

Russell AB, Peterson SB & Mougous JD (2014) Type VI secretion system effectors: Poisons with a purpose. *Nat. Rev. Microbiol.* **12:** 137–148

Scheres SHWW (2012) RELION: implementation of a Bayesian approach to cryo-EM structure determination. *J. Struct. Biol.* **180:** 519–30

Schneider CA, Rasband WS & Eliceiri KW (2012) NIH Image to ImageJ: 25 years of image analysis. *Nat. Methods* **9:** 671–5

Shneider MM, Buth SA, Ho BT, Basler M, Mekalanos JJ & Leiman PG (2013) PAAR-repeat proteins sharpen and diversify the type VI secretion system spike. *Nature* **500:** 350–353

Silverman JM, Agnello DM, Zheng H, Andrews BT, Li M, Catalano CE, Gonen T & Mougous JD (2013) Haemolysin Coregulated Protein Is an Exported Receptor and Chaperone of Type VI Secretion Substrates. *Mol. Cell*

Smart OS, Neduvelil JG, Wang X, Wallace BA & Sansom MSP (1996) HOLE: A program for the analysis of the pore dimensions of ion channel structural models. *J. Mol. Graph.* **14:** 354–360

Spagnuolo J, Opalka N, Wen WX, Gagic D, Chabaud E, Bellini P, Bennett MD, Norris GE, Darst SA, Russel M & Rakonjac J (2010) Identification of the gate regions in the primary structure of the secretin pIV. *Mol. Microbiol.* **76:** 133–150

Terwilliger TC, Sobolev O V., Afonine P V & Adams PD (2018) Automated map sharpening by maximization of detail and connectivity. *Acta Crystallogr. Sect. D Struct. Biol.* **74:** 545–559

Unterweger D, Kostiuk B & Pukatzki S (2017) Adaptor Proteins of Type VI Secretion System Effectors. *Trends Microbiol.* **25:** 8–10

Wang J, Brackmann M, Castaño-Díez D, Kudryashev M, Goldie KN, Maier T, Stahlberg H & Basler M

(2017) Cryo-EM structure of the extended type VI secretion system sheath-tube complex. *Nat. Microbiol.* **2:** 1507–1512

Wang RY-R, Song Y, Barad BA, Cheng Y, Fraser JS & DiMaio F (2016) Automated structure refinement of macromolecular assemblies from cryo-EM maps using Rosetta. *Elife* **5:**

Wang X, Sun B, Xu M, Qiu S, Xu D, Ran T, He J & Wang W (2018) Crystal structure of the periplasmic domain of TssL, a key membrane component of Type VI secretion system. *Int. J. Biol. Macromol.* **120:** 1474–1479

Weiss GL, Medeiros JM & Pilhofer M (2017) In situ imaging of bacterial secretion systems by electron cryotomography. In *Methods in Molecular Biology* pp 353–375.

Yan Z, Yin M, Xu D, Zhu Y & Li X (2017) Structural insights into the secretin translocation channel in the type II secretion system. *Nat. Struct. Mol. Biol.* **24:** 177–183

Zaslaver A, Bren A, Ronen M, Itzkovitz S, Kikoin I, Shavit S, Liebermeister W, Surette MG & Alon U (2006) A comprehensive library of fluorescent transcriptional reporters for Escherichia coli. *Nat. Methods* **3:** 623–628

Zhang K (2016) Gctf: Real-time CTF determination and correction. *J. Struct. Biol.* **193:** 1–12

Zhao W, Caro F, Robins W & Mekalanos JJ (2018) Antagonism toward the intestinal microbiota and its effect on Vibrio cholerae virulence. *Science (80-.).* **359:** 210–213

Zheng SQ, Keszthelyi B, Branlund E, Lyle JM, Braunfeld MB, Sedat JW & Agard DA (2007) UCSF tomography: An integrated software suite for real-time electron microscopic tomographic data collection, alignment, and reconstruction. *J. Struct. Biol.* **157:** 138–147

Zheng SQ, Palovcak E, Armache J-P, Verba KA, Cheng Y & Agard DA (2017) MotionCor2: anisotropic correction of beam-induced motion for improved cryo-electron microscopy. *Nat. Methods* **14:** 331–332

Zoued A, Cassaro CJ, Durand E, Douzi B, España AP, Cambillau C, Journet L & Cascales E (2016) Structure–Function Analysis of the TssL Cytoplasmic Domain Reveals a New Interaction between the Type VI Secretion Baseplate and Membrane Complexes. *J. Mol. Biol.* **428:** 4413–4423

Zoued A, Duneau JP, Durand E, España AP, Journet L, Guerlesquin F & Cascales E (2018) Tryptophan-mediated Dimerization of the TssL Transmembrane Anchor Is Required for Type VI Secretion System Activity. *J. Mol. Biol.*

Zoued A, Durand E, Bebeacua C, Brunet YR, Douzi B, Cambillau C, Cascales E & Journet L (2013) TssK is a trimeric cytoplasmic protein interacting with components of both phage-like and membrane anchoring complexes of the type VI secretion system. *J. Biol. Chem.* **288:** 27031–27041

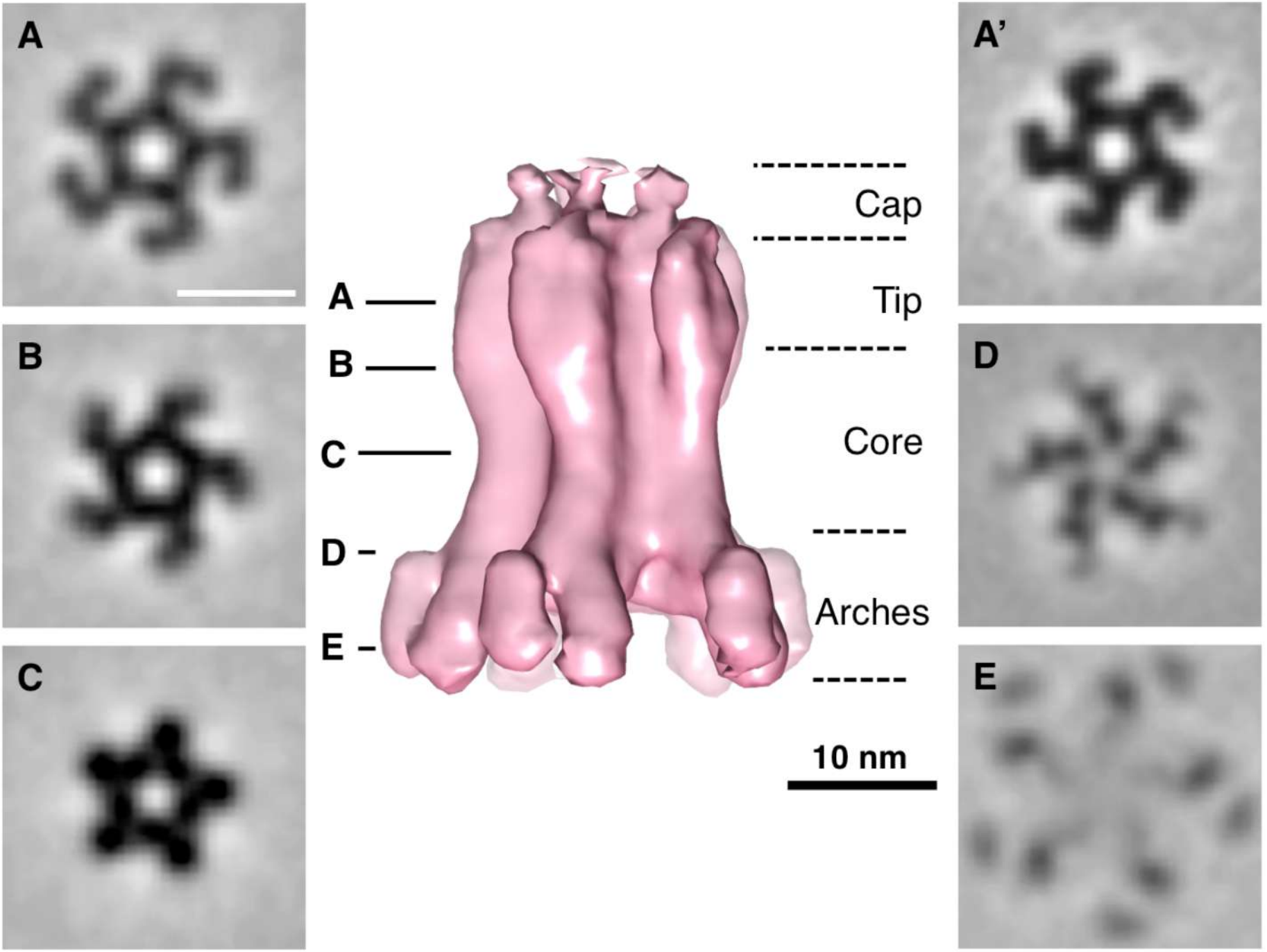
A
A'
B
D
C
E
A
B
C
D
E
Cap
Tip
Core
Arches
10 nm

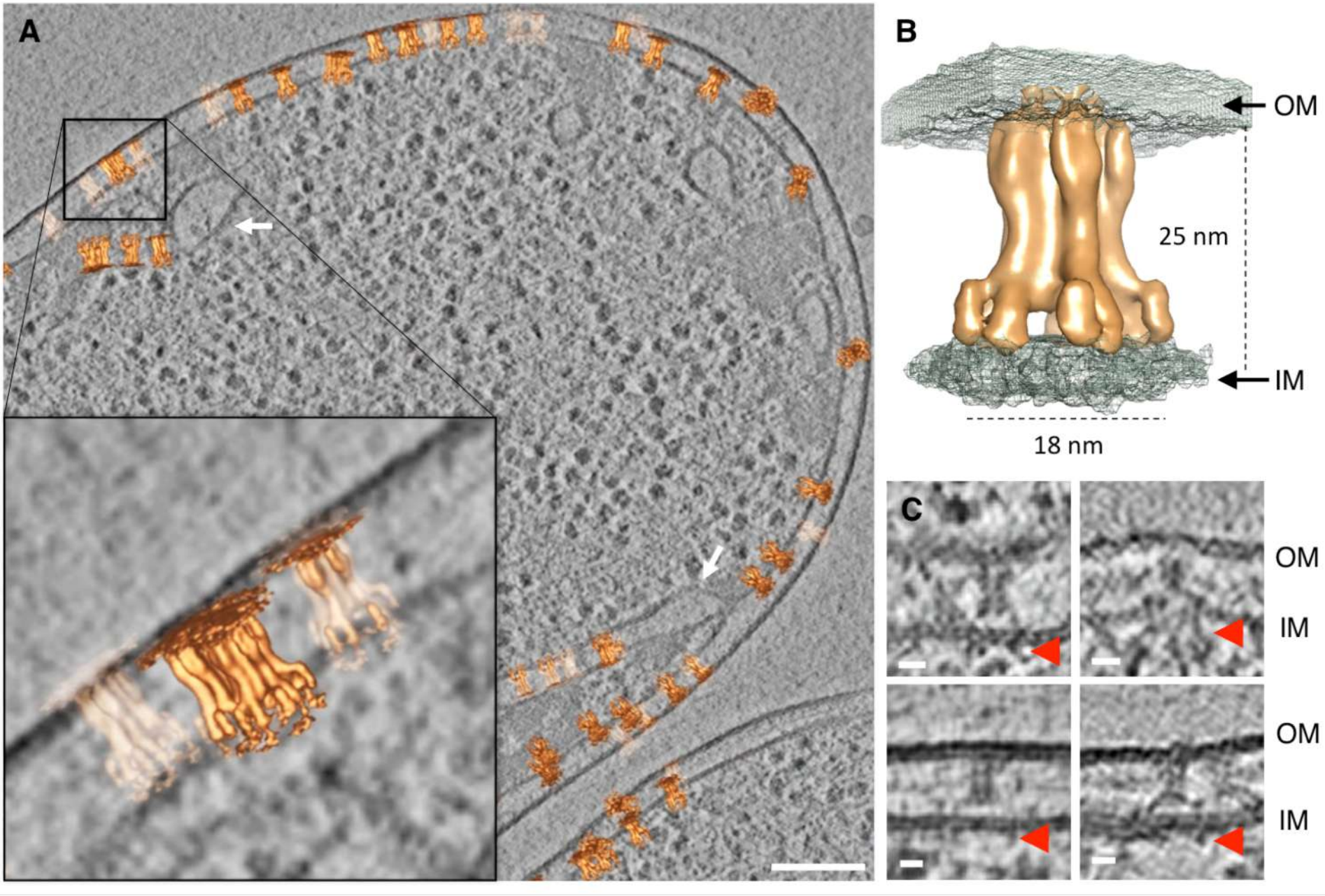
A
B
OM
25 nm
IM
18 nm
C
OM
IM
OM
IM

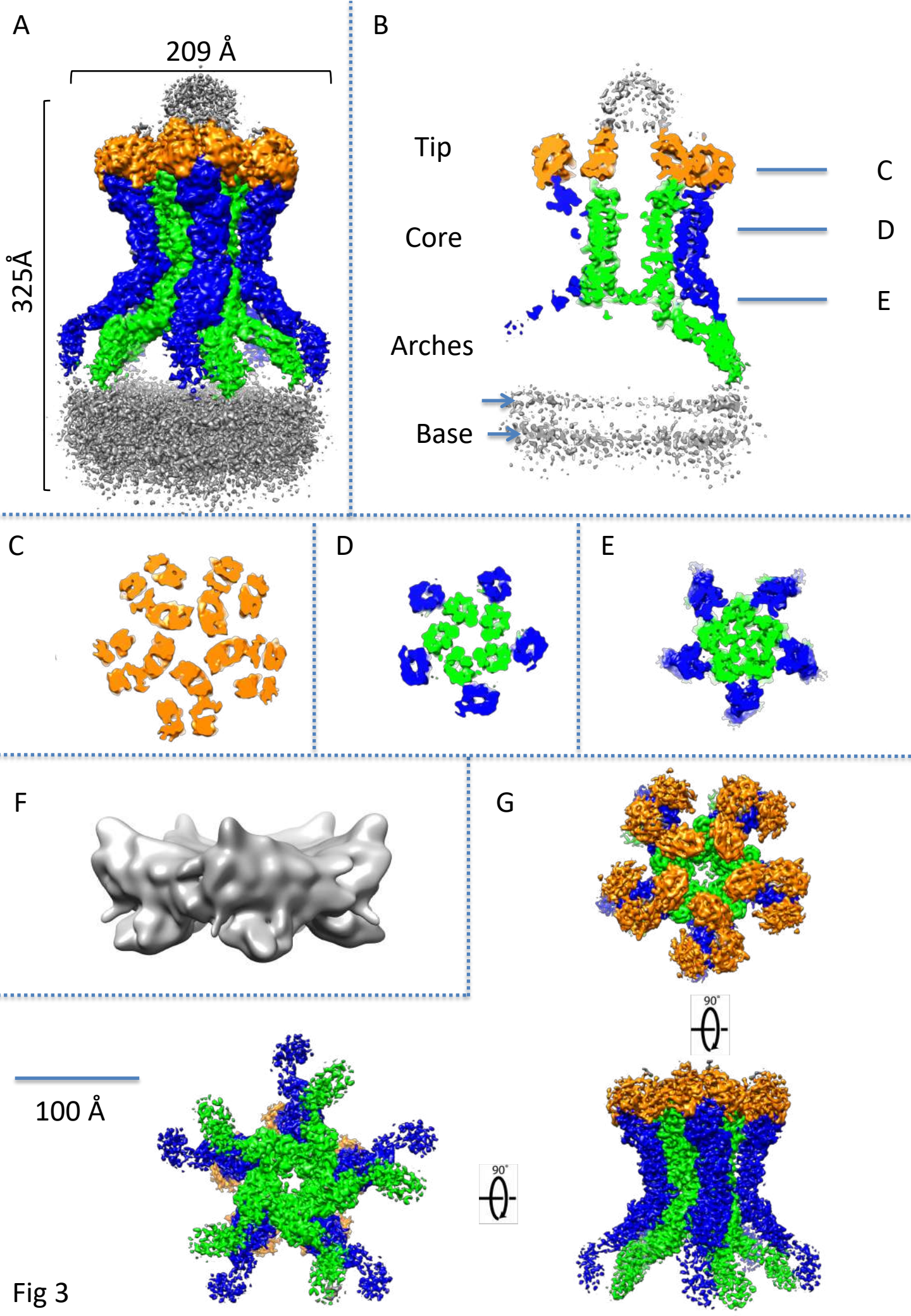

Fig 3

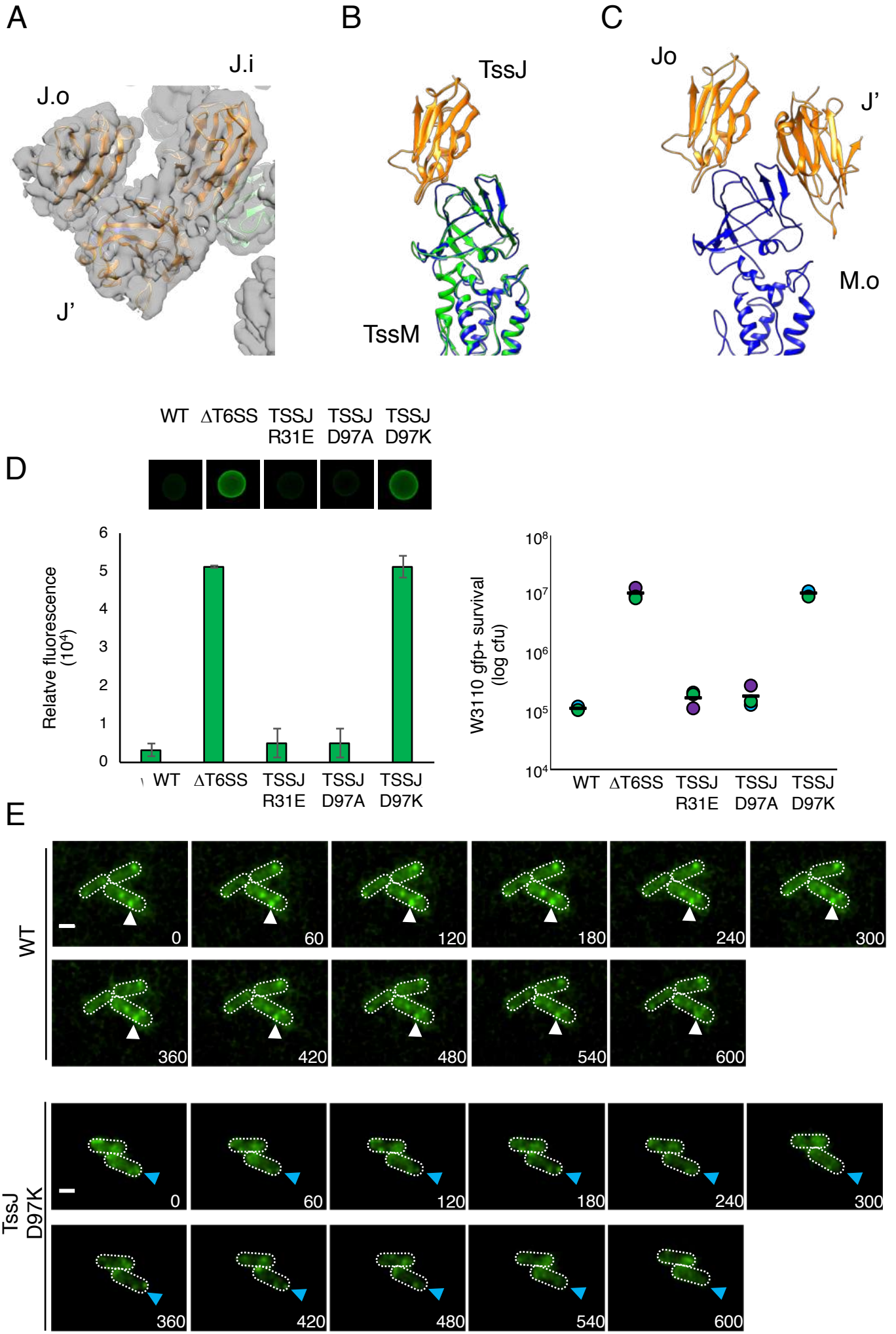
A
J.i
J.o
J'
B
TssJ
TssM
C
Jo
J'
M.o
WT
ΔT6SS
TSSJ R31E
TSSJ D97A
TSSJ D97K
D
Relative fluorescence (10⁴)
W3110 gfp+ survival (log cfu)
E
WT
TssJ D97K
0
60
120
180
240
300
360
420
480
540
600

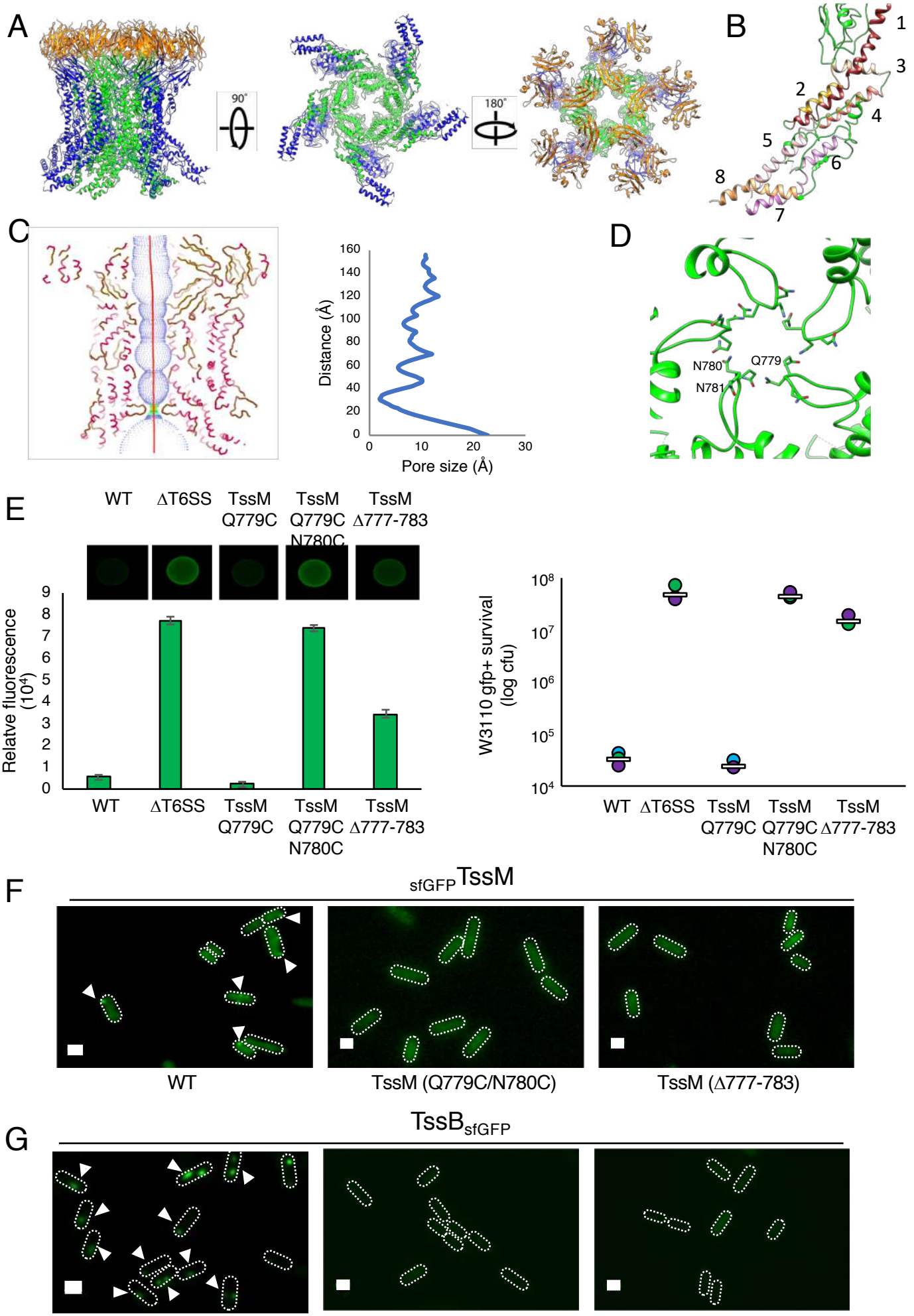
A
90°
180°
B
1
2
3
4
5
6
7
8
C
Distance (Å)
Pore size (Å)
D
N780
Q779
N781
E
WT
ΔT6SS
TssM Q779C
TssM Q779C N780C
TssM Δ777-783
Relative fluorescence (10⁴)
W3110 gfp+ survival (log cfu)
F
sfGFPTssM
WT
TssM (Q779C/N780C)
TssM (Δ777-783)
G
TssBsfGFP
WT
TssM (Q779C/N780C)
TssM (Δ777-783)

Figure 5

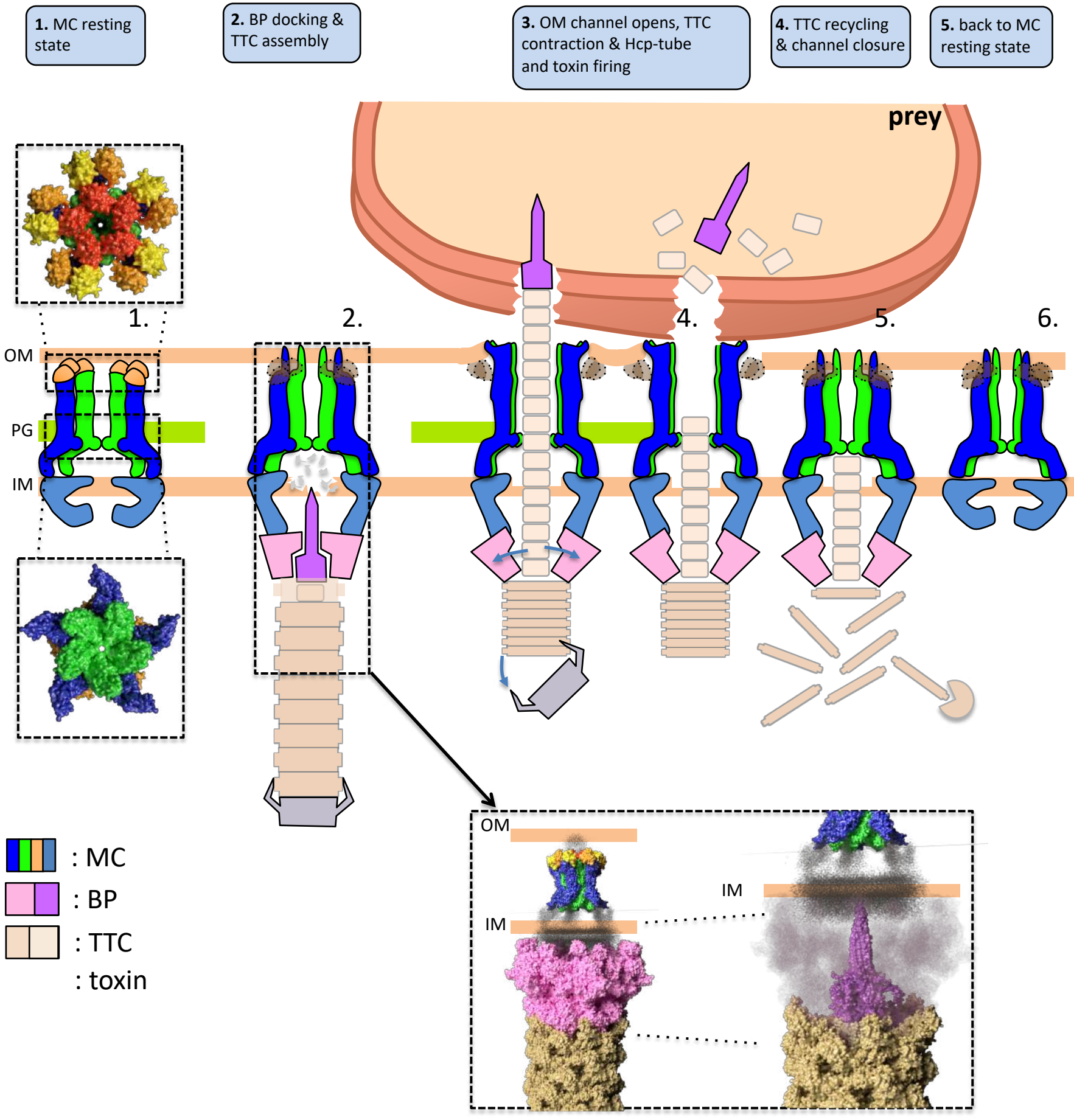
1. MC resting state
2. BP docking & TTC assembly
3. OM channel opens, TTC contraction & Hcp-tube and toxin firing
4. TTC recycling & channel closure
5. back to MC resting state
prey
1.
2.
4.
5.
6.
OM
PG
IM
: MC
: BP
: TTC
: toxin
OM
IM
IM

Expanded view Figure 1

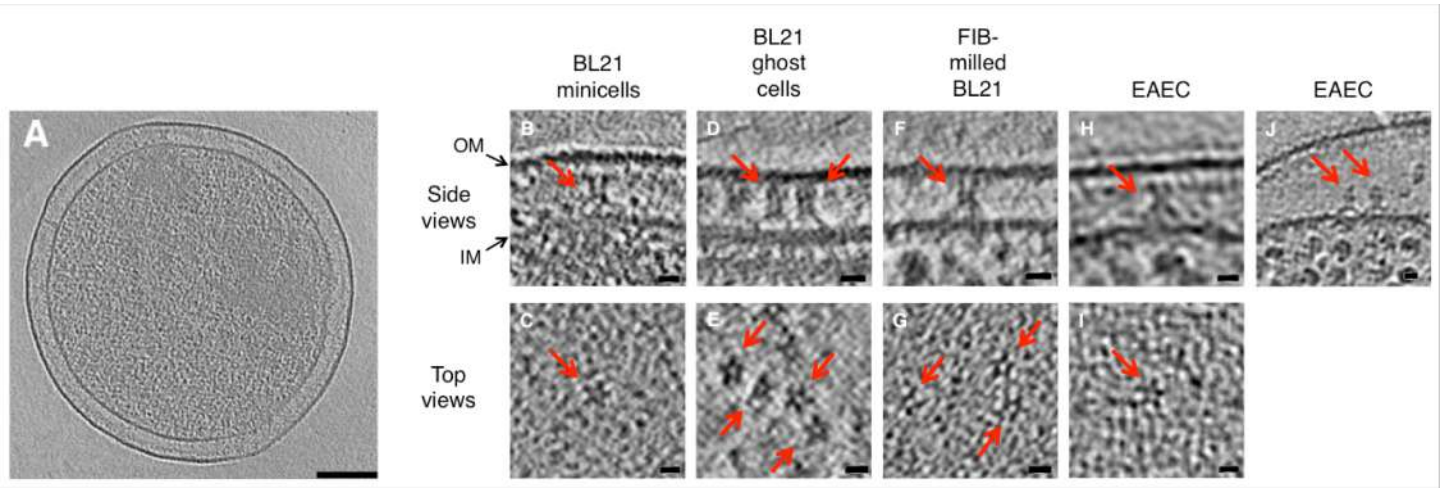

Expanded view Figure 2

A

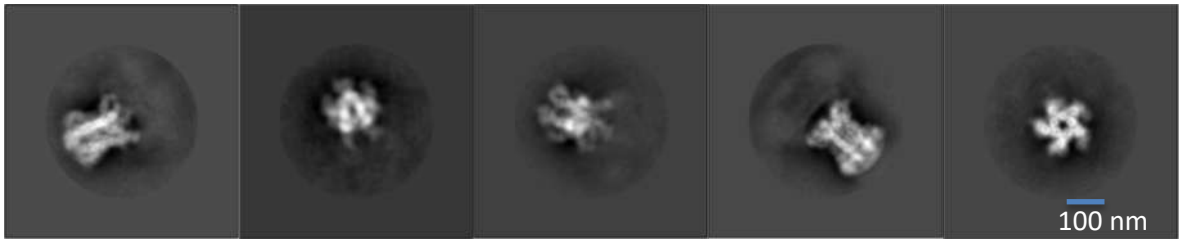

B

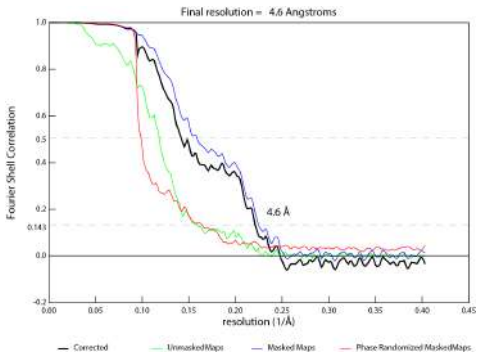

C

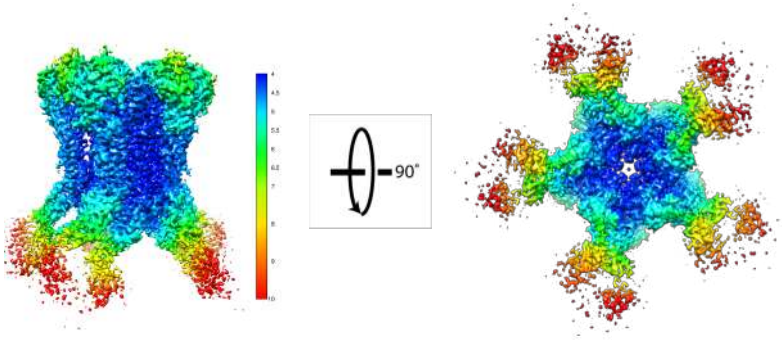

D

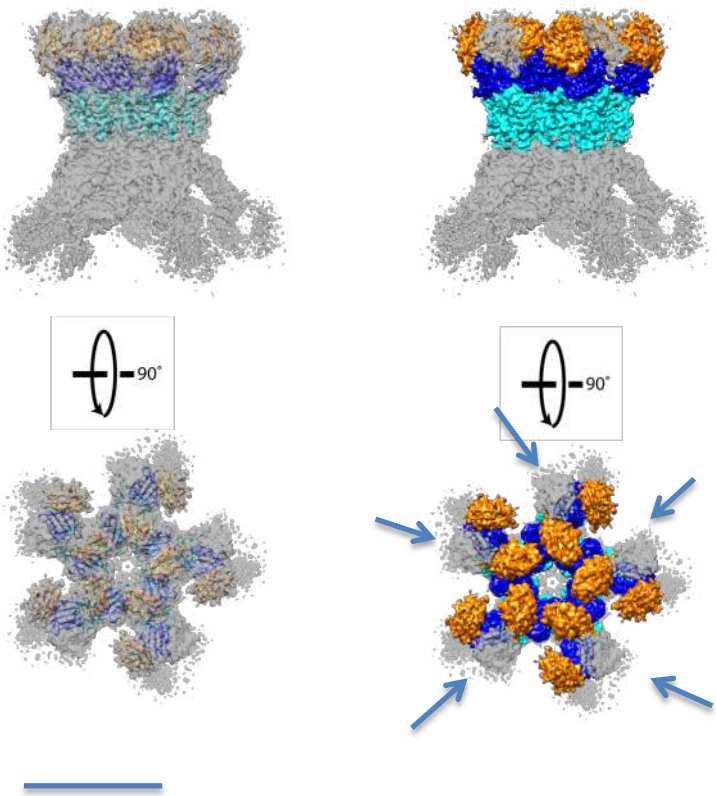

E

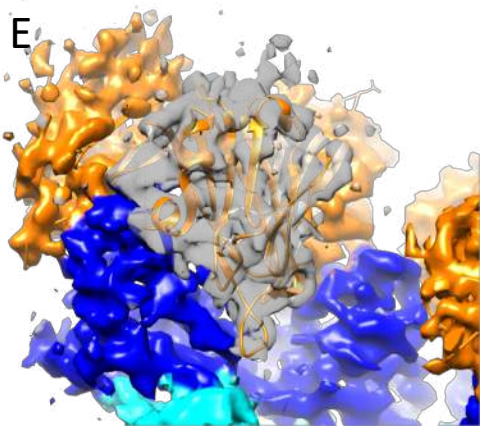

F

27-33

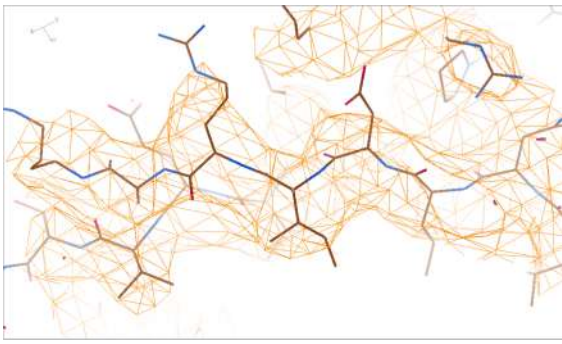

Expanded view Figure 3

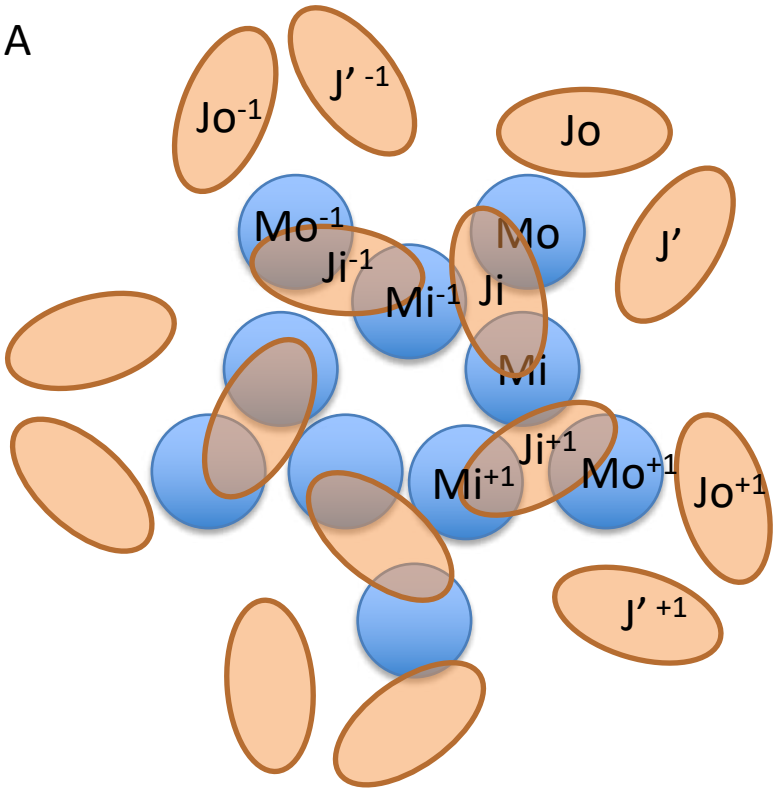

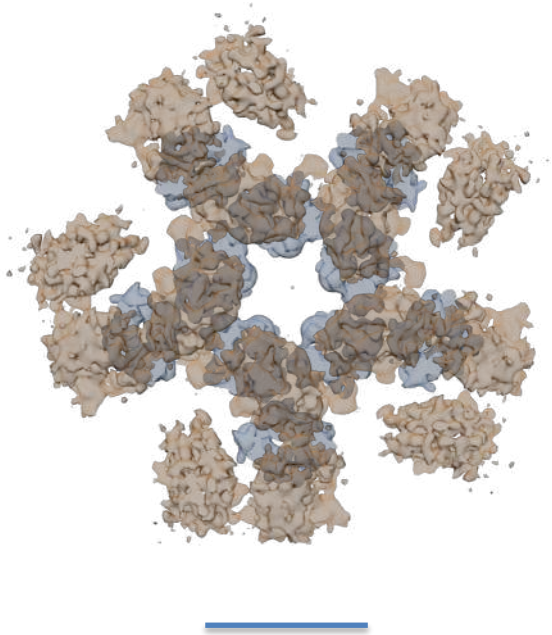

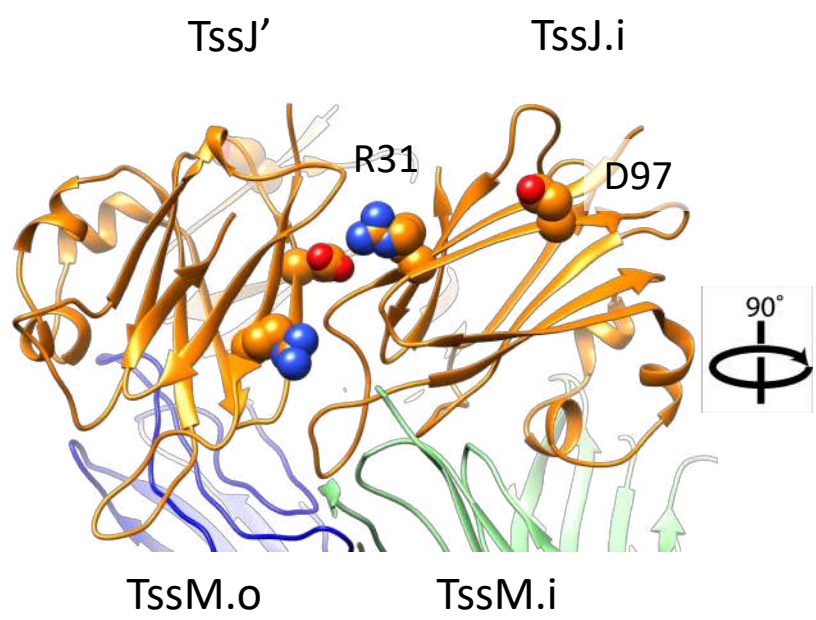

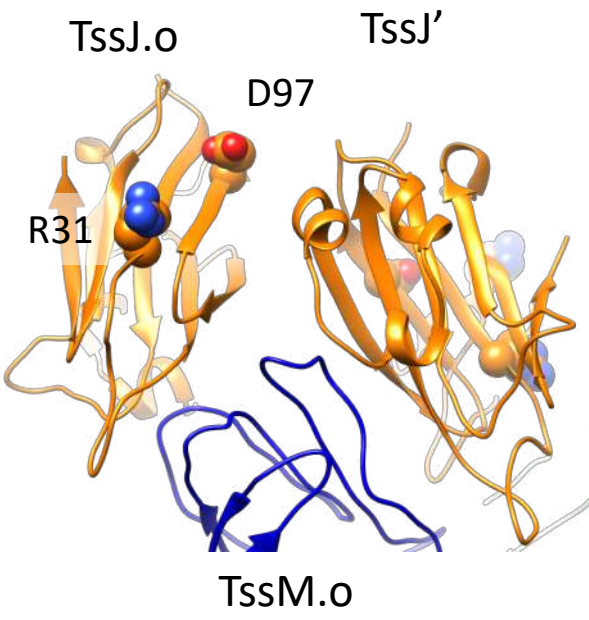

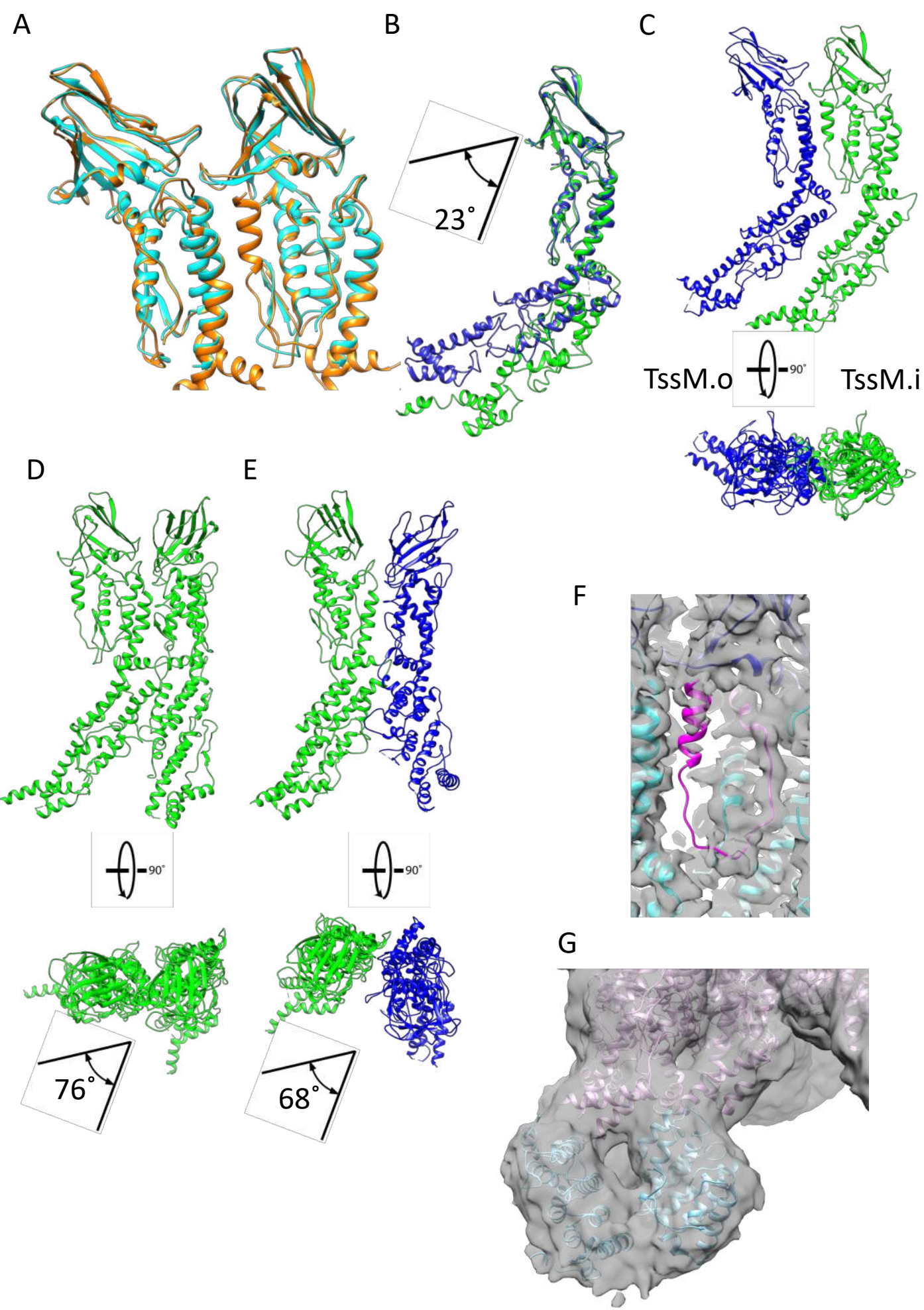

Expanded view Figure 4